JGR Solid Earth

RESEARCH ARTICLE
10.1029/2023JB027454

Topography-Incorporated Adjoint-State Surface Wave Traveltime Tomography: Method and a Case Study in Hawaii

Shijie Hao[1], Jing Chen[1], Mijian Xu[1], and Ping Tong[1,2,3]

[1]Division of Mathematical Sciences, School of Physical and Mathematical Sciences, Nanyang Technological University, Singapore, Singapore, [2]Earth Observatory of Singapore, Nanyang Technological University, Singapore, Singapore, [3]Asian School of the Environment, Nanyang Technological University, Singapore, Singapore

Key Points:

- An elliptically anisotropic eikonal equation is used to model the traveltime fields of surface waves on an undulated topography
- An adjoint-state surface wave tomography method based on the anisotropic eikonal equation is developed to determine shear wave velocity
- The case study in Hawaii suggests limited topography influence on velocity anomaly amplitudes in regions comparable or larger than Hawaii

Supporting Information:

Supporting Information may be found in the online version of this article.

Correspondence to:

P. Tong,
tongping@ntu.edu.sg

Citation:

Hao, S., Chen, J., Xu, M., & Tong, P. (2024). Topography-incorporated adjoint-state surface wave traveltime tomography: Method and a case study in Hawaii. *Journal of Geophysical Research: Solid Earth*, *129*, e2023JB027454. https://doi.org/10.1029/2023JB027454

Received 12 JUL 2023
Accepted 24 DEC 2023

Author Contributions:

Conceptualization: Ping Tong
Data curation: Shijie Hao
Formal analysis: Shijie Hao
Funding acquisition: Ping Tong
Methodology: Shijie Hao, Jing Chen, Ping Tong
Project Administration: Ping Tong
Resources: Ping Tong
Software: Shijie Hao, Mijian Xu
Supervision: Ping Tong
Validation: Shijie Hao
Visualization: Shijie Hao
Writing – original draft: Shijie Hao
Writing – review & editing: Jing Chen, Ping Tong

Abstract In this study we recast surface wave traveltime tomography as an inverse problem constrained by an eikonal equation and solve it using the efficient adjoint-state method. Specifically, recognizing that large topographic variations and high surface wave frequencies can make the topographic effect too significant to ignore, we employ an elliptically anisotropic eikonal equation to describe the traveltime fields of surface waves on undulated topography. The sensitivity kernel of the traveltime objective function with respect to shear wave velocity is derived using the adjoint-state method. As a result, the newly developed method is inherently applicable to any study regions, whether with or without significant topographic variations. Hawaii is one of the most seismically and magmatically active regions. However, its significant topographic variations have made it less accurate to investigate using conventional surface wave traveltime tomography methods. To tackle this problem, we applied our new method to invert ambient noise Rayleigh wave phase traveltimes and construct a 3D shear wave velocity model. Our results reveal features that are consistent with geological structures and previous tomography results, including high velocities below Mauna Loa Volcano and Kilauea Volcano, and low velocities beneath the Hilina Fault Zone. Additionally, our model reveals a high-velocity anomaly to the South of Hualalai's summit, which may be related to a buried rift zone. Our findings further demonstrate that including topography can lead to a correction of up to 0.8% in the shear wave velocity model of Hawaii, an island spanning approximately 100 km with volcanoes reaching elevations exceeding 4 km.

Plain Language Summary Surface wave traveltime tomography is a commonly used technique for constructing subsurface shear wave velocity models based on surface wave traveltime measurements, which has been widely used to investigate the structures of the crust and upper mantle. The accuracy of tomography relies on effective forward modeling, that is, computing traveltime fields in a given velocity model. In this study, we employ an elliptically anisotropic eikonal equation to model the traveltime fields of surface waves on undulated topography, ensuring precise forward modeling in regions with significant topographic variations. The inversion of surface wave traveltimes is formulated as an optimization problem constrained by this elliptically anisotropic eikonal equation, which is solved using the efficient adjoint-state method. We have applied the new tomography method to the Island of Hawaii. High shear wave velocities are revealed beneath the summits and rift zones of Mauna Loa Volcano and Kilauea Volcano, outlining the subsurface structures associated with magma storage and transportation.

1. Introduction

Surface wave tomography is an important imaging technique that has extensive applications in the study of subsurface structures spanning various scales, ranging from tens of meters to thousands of kilometers. Various surface wave tomography methods have been developed, among which the dispersion-based methods are particularly effective in achieving a balance between accuracy and computational efficiency. Such methods have been broadly used in both earthquake data tomography and ambient noise tomography (Barmin et al., 2001; Bensen et al., 2007). They continue to be prevalent in pioneering research, leveraging advancements in seismic observation methodologies and dispersion extraction techniques, such as distributed acoustic sensing (DAS) array data (e.g., J. Fang et al., 2022), dense short period array data (e.g., Castellanos & Clayton, 2021), and higher-mode Rayleigh wave dispersion curves (e.g., J. Wang et al., 2019; Wei et al., 2023).

Surface wave tomography methods for inverting dispersion curves have been developed based on the assumption that the observations reflect the average structures along the propagation paths (Barmin et al., 2001; Ritzwoller &

Levshin, 1998). Hence, accurate modeling of surface wave propagation is essential for the reliability of inversion results. At short periods (<50 s), finite frequency effects are relatively insignificant, thus justifying the eikonal equation as an appropriate approximation for modeling surface wave traveltimes (F.-C. Lin & Ritzwoller, 2011). Moreover, exploiting the fact that surface waves propagate along the Earth's surface, their traveltime fields can be effectively sampled by employing a dense seismic array. This property was leveraged in a study by F.-C. Lin et al. (2009) to directly estimate surface wave slowness by interpolating the traveltime fields using the eikonal equation. In a recent development, H. Fang et al. (2015) developed a one-step inversion method for surface wave analysis. Unlike traditional methods that require phase or group velocity maps, this method directly inverts dispersion curves to construct a 3D model of shear wave velocity (Vs), while the surface wave propagation paths can be determined by solving a 2D eikonal equation (Rawlinson & Sambridge, 2004). Cruz-Hernández et al. (2022) demonstrated that directly inverting for a 3D shear wave velocity model, as opposed to conventional point-wise inversion, can reduce artifacts at larger depths.

The propagation paths of surface waves are influenced by not only horizontal velocity heterogeneity but also topographic variations. Ignoring vertical variations in propagation paths can lead to the underestimation of actual propagation distances, potentially resulting in underestimated velocities. Köhler et al. (2012) argued that the bias introduced by topography has negligible impact on the recovered velocity model in the frequency bands typically used in conventional ambient noise tomography (>3s). Recent advancements in seismic observation techniques have facilitated the deployment of dense seismic arrays, enabling the utilization of higher-frequency data in seismic interferometry (e.g., F.-C. Lin et al., 2013). To obtain reliable surface wave tomography results using high-frequency data, it is essential to take into account and correct for the effects of topography variations. By utilizing a suitable numerical scheme, such as the spectral element method (Komatitsch & Tromp, 1999), and implementing a proper boundary condition along the topographic surface, wave equation-based tomography methods can naturally account for the impact of surface topography (e.g., Borisov et al., 2018; Li et al., 2019; K. Wang et al., 2021). Despite this, due to the computational efficiency and simplicity of dispersion-based surface wave tomography methods, there are ongoing efforts to address the effects of topography within these methods. For instance, Zhao et al. (2020) computed a correction term by comparing the group velocities between a 3D simulation that incorporates surface topography and a 1D simulation that neglects topography effects. Their approach resulted in an improved Vs model. However, the correction term should ideally vary throughout the iterative inversion process, but in this case, it remained constant. In a separate investigation, Jin et al. (2022) examined the topography effects in the Longmenshan area and developed a first-order correction formula based on SPECFEM3D simulations.

The adjoint-state method is a versatile technique that can efficiently compute the gradient of a functional in terms of state variables, such as the objective functions found in inverse problems, where the state variables typically represent the solutions of forward problems (Fichtner et al., 2006; Tromp et al., 2005). The adjoint-state method has been introduced to solve various seismic inverse problems based on eikonal equations, including local earthquake tomography (e.g., Leung & Qian, 2006; Taillandier et al., 2009; Tong, 2021a), body-wave differential arrival time tomography (e.g., Tavakoli et al., 2017; Tong et al., 2024) and seismic anisotropy tomography (Tong, 2021b). It is also feasible for teleseismic traveltime tomography (Chen et al., 2023). In this study, we develop a novel approach called adjoint-state surface wave traveltime tomography, which enables the inversion of surface wave traveltimes while inherently accounting for the topography effects. This method utilizes an elliptically anisotropic eikonal equation to accurately model the traveltime fields of surface waves on undulated topography, while the corresponding tomographic inversion problem is solved by the efficient adjoint-state method. We apply this method to investigate crustal structures beneath Hawaii Island, known for its significant topographic variations that may cause inaccuracy for surface wave tomography. Finally, a crustal Vs model is obtained, and its geological implications are discussed.

2. Methodology

The goal of adjoint-state surface wave traveltime tomography is to find an optimal Vs model that can minimize the misfit between observed and simulated surface wave traveltimes. This process typically involves utilizing a gradient-based iterative algorithm to obtain an optimal model. In this discussion, we will focus on the following aspects in detail: (a) Simulating the traveltimes of surface waves given a specific phase velocity and topography setup; (b) Deriving the Fréchet derivative of the misfit function with respect to surface wave phase velocity; (c)

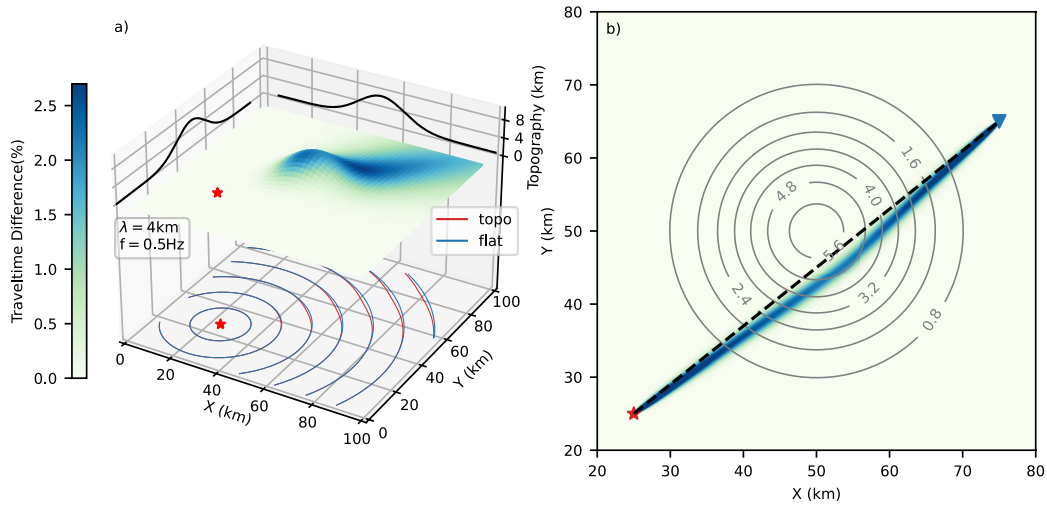

Figure 1. (a) Surface wave traveltimes on the curved surface of a homogeneous velocity model, where the wavelength and frequency of the surface wave are 4.0 km and 0.5 Hz, respectively. The source is denoted by red stars. Curved surface illustrates the topography. The traveltime contours on this curved surface are depicted by red lines, while those on a flat surface are demonstrated by blue lines. Differences between the traveltimes calculated on flat and curved surfaces are highlighted using background colors. (b) An adjoint field calculated in the same condition as (a). The gray lines are contours of the topography, the star and triangle denote the source and receiver, respectively. The black dashed line is a straight-line connecting the source and receiver, serving as a reference for how topographic variations distort the propagation path of surface waves.

Deriving the Fréchet derivative of the misfit function with respect to shear wave velocity; (d) Parameterizing and optimizing the velocity model. While our derivation is primarily based on phase velocity, it is also applicable to group velocity.

2.1. Eikonal Equation Considering Topography

We consider N seismic sources (earthquakes or virtual sources) located at $\boldsymbol{x}_{s,n}$ ($n = 1, 2, \ldots, N$). When surface waves of a specific frequency propagate along a flat surface, their traveltime field $T_{n,f}$ (f denotes frequency, $f \in \mathcal{F}$, with $\mathcal{F}$ being the set of measured frequencies) can be described by the 2D eikonal equation:

$$\begin{cases} \left[\nabla T_{n,f}\left(\boldsymbol{x}^{\mathbf{0}}\right)\right]^{t} \nabla T_{n,f}\left(\boldsymbol{x}^{\mathbf{0}}\right) = s_f^2\left(\boldsymbol{x}^{\mathbf{0}}\right), \\ T_{n,f}(\boldsymbol{x}_{s,n}) = 0, \end{cases} \tag{1}$$

where t represents transposition, $\boldsymbol{x}^{\mathbf{0}} = (x, y)$ is any location at the Earth's surface (depth is zero), and s_f denotes the surface wave phase slowness at frequency f. When surface waves propagate along a curved surface with topographic variation $z = \Phi(\boldsymbol{x}^{\mathbf{0}})$, their traveltime field can be modeled by the following elliptically anisotropic eikonal equation (Appendix A):

$$\begin{cases} \left[\nabla T_{n,f}\left(\boldsymbol{x}^{\mathbf{0}}\right)\right]^{t} \begin{bmatrix} a\left(\boldsymbol{x}^{\mathbf{0}}\right) & -c\left(\boldsymbol{x}^{\mathbf{0}}\right) \\ -c\left(\boldsymbol{x}^{\mathbf{0}}\right) & b\left(\boldsymbol{x}^{\mathbf{0}}\right) \end{bmatrix} \nabla T_{n,f}\left(\boldsymbol{x}^{\mathbf{0}}\right) = s_f^2\left(\boldsymbol{x}^{\mathbf{0}}\right), \\ T_{n,f}(\boldsymbol{x}_{s,n}) = 0, \end{cases} \tag{2}$$

where a, b, c are parameters related to the curved surface: $a = \frac{1+\Phi_y^2}{\Phi_x^2+\Phi_y^2+1}$, $b = \frac{1+\Phi_x^2}{\Phi_x^2+\Phi_y^2+1}$, $c = \frac{\Phi_x\Phi_y}{\Phi_x^2+\Phi_y^2+1}$, ($\Phi_x = \frac{\partial\Phi}{\partial x}$, $\Phi_y = \frac{\partial\Phi}{\partial y}$). It is obvious that Equation 2 degenerates to Equation 1 in the case of a flat surface, where $\Phi(\boldsymbol{x}^{\mathbf{0}})$ is a constant. Figure 1a provides an illustrative example of how the inclusion of topography via Equation 2 can affect the traveltime field.

To simulate surface wave propagation over a topographic surface using Equation 2, we can equate $\Phi(\boldsymbol{x}^{\mathbf{0}})$ to the topography. However, high resolution topographic data may include local variations with small amplitudes and

short wavelengths. It may be unreasonable to assume that surface waves with longer wavelengths propagate totally along these minor topographic variations. To avoid overestimating the propagation distance of surface waves, a low-pass filter can be applied to the topography, with the corner wavelength of the filter ($\lambda_{filter,f}$) determined by the surface wave's wavelength at the corresponding frequency ($\lambda_{wave,f}$). This relationship is given by $\lambda_{filter,f} = \kappa\lambda_{wave,f}$, where κ is a factor. Waveform simulations have indicated that setting $\kappa = 2.5$ is more effective in accommodating the bias induced by topography compared to other values (Köhler et al., 2012).

2.2. Fréchet Derivative With Respect to Surface Wave Velocity

Surface wave phase traveltimes between sources and receivers can be extracted from surface wave waveforms. Consider N sources located at $\boldsymbol{x}_{s,n}$ (n = 1, 2, …, N) and M receivers located at $\boldsymbol{x}_{r,m}$ (m = 1, 2, …, M). The frequency-dependent objective function for surface wave traveltime tomography can be defined as:

$$\chi_f\left(s_f\left(\boldsymbol{x}^{\mathbf{0}}\right)\right) = \sum_{n=1}^{N}\sum_{m=1}^{M}\frac{\omega_{n,m,f}}{2}\left[T_{n,f}(\boldsymbol{x}_{r,m}) - T^{o}_{n,f}(\boldsymbol{x}_{r,m})\right]^2, \tag{3}$$

where $\omega_{n,m,f}$ is a weighting factor for the traveltime observation corresponding to the nth source and mth receiver, $T_{n,f}(\boldsymbol{x}_{r,m})$ is the calculated traveltime in the surface wave phase slowness model $s_f(\boldsymbol{x}^{\mathbf{0}})$, and $T^{o}_{n,f}(\boldsymbol{x}_{r,m})$ is the observed traveltime. Assume an infinitesimal perturbation in the phase slowness $\delta s_f(\boldsymbol{x}^{\mathbf{0}})$. Then the resulting traveltime field perturbation is $\delta T_{n,f}(\boldsymbol{x}^{\mathbf{0}})$. The perturbed phase slowness $s_f + \delta s_f$ and perturbed traveltime field $T_{n,f} + \delta T_{n,f}$ satisfy the following eikonal equation:

$$\left[\nabla(T_{n,f} + \delta T_{n,f})\right]^t\begin{bmatrix} a & -c \\ -c & b \end{bmatrix}\nabla(T_{n,f} + \delta T_{n,f}) = (s_f + \delta s_f)^2. \tag{4}$$

Meanwhile, under the first-order approximation, the perturbation of the objective function can be approximated by:

$$\begin{aligned}\delta\chi_f\left(s_f\left(\boldsymbol{x}^{\mathbf{0}}\right)\right) &= \sum_{n=1}^{N}\sum_{m=1}^{M}\omega_{n,m,f}\left[T_{n,f}(\boldsymbol{x}_{r,m}) - T^{o}_{n,f}(\boldsymbol{x}_{r,m})\right]\delta T_{n,f}(\boldsymbol{x}_{r,m}) \\ &= \sum_{n=1}^{N}\int_D\sum_{m=1}^{M}\omega_{n,m,f}\left[T_{n,f}\left(\boldsymbol{x}^{\mathbf{0}}\right) - T^{o}_{n,f}(\boldsymbol{x}_{r,m})\right]\delta T_{n,f}\left(\boldsymbol{x}^{\mathbf{0}}\right)\delta\left(\boldsymbol{x}^{\mathbf{0}} - \boldsymbol{x}_{r,m}\right)d\boldsymbol{x}^{\mathbf{0}},\end{aligned} \tag{5}$$

where D is the research region on the Earth's surface, $\delta(\boldsymbol{x}^{\mathbf{0}} - \boldsymbol{x}_{r,m})$ is the Dirac delta function.

Subtracting Equation 2 from Equation 4 and ignoring second-order terms, we have:

$$\left[\nabla T_{n,f}\right]^t\begin{bmatrix} a & -c \\ -c & b \end{bmatrix}\nabla\delta T_{n,f} = s_f\delta s_f. \tag{6}$$

Multiply an arbitrary test function $P_{n,f}(\boldsymbol{x}^{\mathbf{0}})$ on both sides of Equation 6 and integrate over the research region D:

$$\int_D P_{n,f}\left[\nabla T_{n,f}\right]^t\begin{bmatrix} a & -c \\ -c & b \end{bmatrix}\nabla\delta T_{n,f}\,d\boldsymbol{x}^{\mathbf{0}} = \int_D P_{n,f}s_f\delta s_f\,d\boldsymbol{x}^{\mathbf{0}}. \tag{7}$$

If $P_{n,f} = 0$ is assumed on the boundary of the research region D, then the left-hand side of Equation 7 can be simplified using the divergence theorem:

$$\begin{aligned}\text{LHS} &= \int_D P_{n,f}\left[\nabla T_{n,f}\right]^t \begin{bmatrix} a & -c \\ -c & b \end{bmatrix} \nabla \delta T_{n,f} d\boldsymbol{x}^{\mathbf{0}} \\ &= \int_D \nabla \cdot \left\{ P_{n,f}\left[\nabla T_{n,f}\right]^t \begin{bmatrix} a & -c \\ -c & b \end{bmatrix} \delta T_{n,f} \right\} d\boldsymbol{x}^{\mathbf{0}} - \int_D \delta T_{n,f} \nabla \cdot \left\{ P_{n,f}\left[\nabla T_{n,f}\right]^t \begin{bmatrix} a & -c \\ -c & b \end{bmatrix} \right\} d\boldsymbol{x}^{\mathbf{0}} \\ &= \int_D \delta T_{n,f} \nabla \cdot \left\{ P_{n,f}\left[-\nabla T_{n,f}\right]^t \begin{bmatrix} a & -c \\ -c & b \end{bmatrix} \right\} d\boldsymbol{x}^{\mathbf{0}}.\end{aligned} \tag{8}$$

We further make a second assumption about $P_{n,f}$:

$$\begin{aligned}&\nabla \cdot \left\{ P_{n,f}\left[-\nabla T_{n,f}\right]^t \begin{bmatrix} a & -c \\ -c & b \end{bmatrix} \right\} = \\ &\sum_{m=1}^{M} \omega_{n,m,f}\left[T_{n,f} - T^o_{n,f}(\boldsymbol{x}_{r,m})\right] \delta(\boldsymbol{x} - \boldsymbol{x}_{r,m}).\end{aligned} \tag{9}$$

An intuitive explanation of Equation 9 is that the adjoint field $P_{n,f}$ describes the backward transportation of the frequency-dependent traveltime residuals from the receivers $\boldsymbol{x}_{r,m}$ along the negative direction of the surface wave propagation to the source $\boldsymbol{x}_{s,n}$. Figure 1b provides an illustrative example on how the adjoint field is influenced by the inclusion of topography. Substituting the right-hand side of Equation 9 into Equation 8 and equating the result to the right-hand side of Equation 7, we obtain:

$$\begin{aligned}&\int_D \delta T_{n,f} \sum_{m=1}^{M} \omega_{n,m,f}\left[T_{n,f} - T^o_{n,f}(\boldsymbol{x}_{r,m})\right] \delta(\boldsymbol{x} - \boldsymbol{x}_{r,m}) d\boldsymbol{x}^{\mathbf{0}} = \\ &\qquad \int_D P_{n,f} s_f \delta s_f d\boldsymbol{x}^{\mathbf{0}}.\end{aligned} \tag{10}$$

Comparing Equation 10 with Equation 5, the perturbation of χ_f is directly related to the perturbation of the surface wave phase slowness s_f,

$$\delta\chi_f(s_f) = \sum_{n=1}^{N} \int_D P_{n,f} s_f^2 \frac{\delta s_f}{s_f} d\boldsymbol{x}^{\mathbf{0}} = \sum_{n=1}^{N} \int_D K^s_{n,f} \frac{\delta s_f}{s_f} d\boldsymbol{x}^{\mathbf{0}} = \int_D K^s_f \frac{\delta s_f}{s_f} d\boldsymbol{x}^{\mathbf{0}}, \tag{11}$$

where $K^s_{n,f} = P_{n,f} s_f^2$ and $K^s_f = \sum_{n=1}^{N} K^s_{n,f}$ are event kernel and misfit kernel, respectively.

Finally, we define an overall objective function by considering multiple frequencies in the frequency set $\mathcal{F}$:

$$\chi = \sum_{f \in \mathcal{F}} \chi_f. \tag{12}$$

2.3. Fréchet Derivative With Respect to Shear Wave Velocity

The variation of the phase slowness s_f can be expressed as the sum of integrals of variations in P-wave velocity α (Vp), shear wave velocity β (Vs), and density ρ along the vertical direction (Appendix C; Aki & Richards, 2002):

$$\begin{aligned}\delta s_f(\boldsymbol{x}^{\mathbf{0}}) &= -\frac{1}{c_f^2(\boldsymbol{x}^{\mathbf{0}})} \delta c_f(\boldsymbol{x}^{\mathbf{0}}) \\ &= -\frac{1}{c_f^2(\boldsymbol{x}^{\mathbf{0}})} \int_0^{\infty} \left[K^{\alpha}_{c,f}(\boldsymbol{x}^{\mathbf{0}}, z) \delta\alpha(\boldsymbol{x}^{\mathbf{0}}, z) + K^{\beta}_{c,f}(\boldsymbol{x}^{\mathbf{0}}, z) \delta\beta(\boldsymbol{x}^{\mathbf{0}}, z) + K^{\rho}_{c,f}(\boldsymbol{x}^{\mathbf{0}}, z) \delta\rho(\boldsymbol{x}^{\mathbf{0}}, z) \right] dz,\end{aligned} \tag{13}$$

where $K^{\alpha}_{c,f}$, $K^{\beta}_{c,f}$, $K^{\rho}_{c,f}$ are kernels of the phase velocity with respect to Vp, Vs, and density, respectively. The detailed expressions of these kernels are presented in Equation C15. Substituting Equation 13 into Equation 11 yields:

$$\begin{aligned}\delta\chi_f &= \int_D -K^s_f(\boldsymbol{x}^0)s_f(\boldsymbol{x}^0)\int_0^{\infty}\left[K^{\alpha}_{c,f}(\boldsymbol{x}^0,z)\delta\alpha(\boldsymbol{x}^0,z)+K^{\beta}_{c,f}(\boldsymbol{x}^0,z)\delta\beta(\boldsymbol{x}^0,z)+K^{\rho}_{c,f}(\boldsymbol{x}^0,z)\delta\rho(\boldsymbol{x}^0,z)\right]dzd\boldsymbol{x}^0 \\ &= \int_{\Omega} -K^s_f(\boldsymbol{x}^0)s_f(\boldsymbol{x}^0)\left[K^{\alpha}_{c,f}(\boldsymbol{x})\delta\alpha(\boldsymbol{x})+K^{\beta}_{c,f}(\boldsymbol{x})\delta\beta(\boldsymbol{x})+K^{\rho}_{c,f}(\boldsymbol{x})\delta\rho(\boldsymbol{x})\right]d\boldsymbol{x},\end{aligned} \tag{14}$$

where $\boldsymbol{x}$ denotes an arbitrary position within the Earth volume. Note that the 2D integration along the lateral study area and the 1D integration in the depth direction have been combined into a 3D integration within the subsurface space Ω. Consequently, the perturbation of the overall misfit function is:

$$\begin{aligned}\delta\chi &= \sum_{f\in F}\delta\chi_f \\ &= \int_{\Omega}\left[K^{\alpha}_c(\boldsymbol{x})\delta\alpha(\boldsymbol{x})+K^{\beta}_c(\boldsymbol{x})\delta\beta(\boldsymbol{x})+K^{\rho}_c(\boldsymbol{x})\delta\rho(\boldsymbol{x})\right]d\boldsymbol{x},\end{aligned} \tag{15}$$

where K^{α}_c, K^{β}_c, K^{ρ}_c are Vp, Vs and density kernels:

$$K^{\alpha}_c(\boldsymbol{x}) = \sum_{f\in F}\left[-K^s_f(\boldsymbol{x}^0)s_f(\boldsymbol{x}^0)\right]K^{\alpha}_{c,f}(\boldsymbol{x}), \tag{16}$$

$$K^{\beta}_c(\boldsymbol{x}) = \sum_{f\in F}\left[-K^s_f(\boldsymbol{x}^0)s_f(\boldsymbol{x}^0)\right]K^{\beta}_{c,f}(\boldsymbol{x}), \tag{17}$$

$$K^{\rho}_c(\boldsymbol{x}) = \sum_{f\in F}\left[-K^s_f(\boldsymbol{x}^0)s_f(\boldsymbol{x}^0)\right]K^{\rho}_{c,f}(\boldsymbol{x}). \tag{18}$$

As commonly observed (e.g., Beaty et al., 2002; Lebedev & Van Der Hilst, 2008), surface wave phase velocity is more sensitive to shear wave velocity. Consequently, it is challenging to independently resolve Vp and density using Rayleigh waves (Lebedev & Van Der Hilst, 2008). In this work, Vp and density are assumed to be dependent on Vs based on empirical relationships:

$$\alpha(\boldsymbol{x}) = h_{\alpha}(\beta(\boldsymbol{x})), \tag{19}$$

$$\rho(\boldsymbol{x}) = h_{\rho}(\beta(\boldsymbol{x})), \tag{20}$$

where h_{α} and h_{ρ} are empirical relationships in the form of polynomials (Equations S1 and S2 in Supporting Information S1), as determined from observations such as borehole logs and laboratory measurements (Brocher, 2005). Substituting the two empirical relationships into Equation 15 gives:

$$\delta\chi = \int_{\Omega} K^{\beta;\alpha,\rho}_c(\boldsymbol{x})\frac{\delta\beta(\boldsymbol{x})}{\beta(\boldsymbol{x})}d\boldsymbol{x}, \tag{21}$$

where $K^{\beta;\alpha,\rho}_c$ is called the integrated Vs kernel and is defined as:

$$K^{\beta;\alpha,\rho}_c(\boldsymbol{x}) = \left[K^{\alpha}_c(\boldsymbol{x})\frac{dh_{\alpha}}{d\beta}+K^{\beta}_c(\boldsymbol{x})+K^{\rho}_c(\boldsymbol{x})\frac{dh_{\rho}}{d\beta}\right]\beta(\boldsymbol{x}). \tag{22}$$

2.4. Inversion Scheme

The perturbation of the overall misfit function can be expressed as a function of the shear wave velocity perturbation, as shown in Equation 21. This relationship enables us to find optimal 3D models of shear wave velocity, P-wave velocity, and density that minimize the overall misfit function. In numerical forward modeling, these models are discretized on a 3D regular fine grid, where the grid sizes are $\Delta x \times \Delta y \times \Delta z$. In a horizontally homogeneous model, surface wave velocities and kernels can be calculated from body wave velocities and densities (as detailed in Appendices B and C). In a 3D heterogeneous model, we can calculate surface wave velocities and kernels at each horizontal location independently, under the assumption of a horizontally

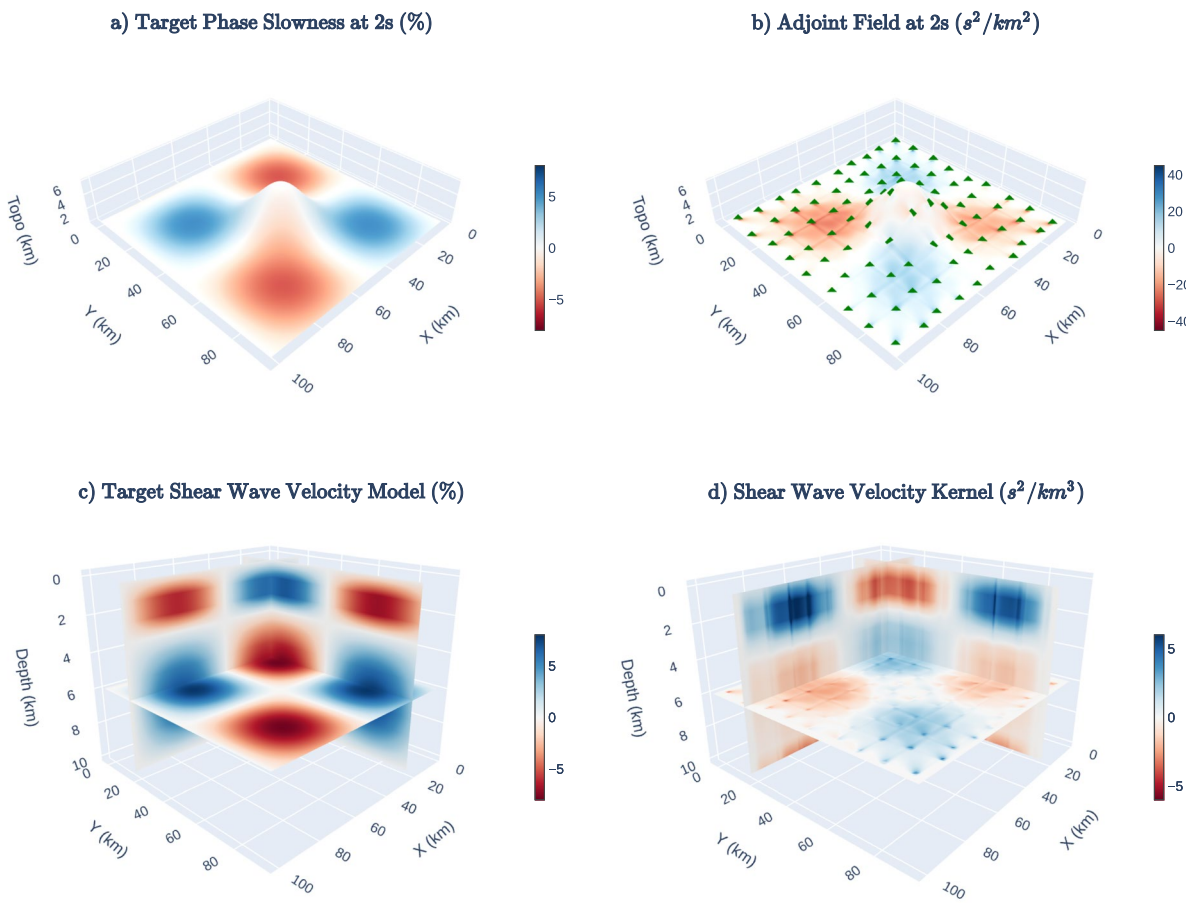

Figure 2. Visualization of the adjoint field and sensitivity kernels. (a) The target surface wave phase slowness at 2s, represented as a perturbation from a constant slowness of 0.51 s/km. (b) The summation of all sources' adjoint fields at 2s. Seismic stations, which act both as receivers and virtual sources, are marked by green triangles. (c) The target model of the shear wave velocity, displayed as a perturbation with respect to an initial model where Vs increases linearly with depth, ranging from 1.8 km/s to 4.0 km/s. (d) The integrated shear wave velocity kernel, calculated for periods between 2 and 9.5 s (Equation 22).

homogeneous model. This approach has been adopted in previous surface wave tomography methods (e.g., H. Fang et al., 2015; Xia, 2014). The eikonal equation (Equation 2) and adjoint equation (Equation 9) are numerically solved using the fast sweeping method (Kao et al., 2005; Tong, 2021b), with the surface wave phase slowness (velocity), adjoint field and traveltime field being discretized on a 2D regular fine grid, whose sizes are $\Delta x \times \Delta y$. Figure 2 illustrates an example of an adjoint field and an integrated shear wave velocity kernel. The adjoint field shows a consistent pattern with the phase slowness perturbations at the corresponding period. The integrated shear wave velocity kernel can resolve Vs variations in both horizontal and vertical directions.

The relative shear wave velocity perturbation $\frac{\delta\beta(\boldsymbol{x})}{\beta(\boldsymbol{x})}$ is interpolated on an inversion grid consisting of multiple regular coarse grids placed in a staggered way (Tong et al., 2019). The grid node of the hth ($h = 1, 2, \ldots, H$) inversion grid is denoted by $\left(X_i^h, Y_j^h, Z_k^h\right)$ with $i = 1, 2, \ldots, N_x$, $j = 1, 2, \ldots, N_y$, and $k = 1, 2, \ldots, N_z$. Each grid node is associated with a basis function B_l^h as:

$$B_l^h(x, y, z) = w_i^h(x) w_j^h(y) w_k^h(z), \tag{23}$$

where $l = (k-1)N_xN_y + (j-1)N_x + i$, and w_i is defined as:

$$w_i^h(x) = \begin{cases} \frac{x - X_{i-1}^h}{X_i^h - X_{i-1}^h}, & \text{if } X_1^h \le X_{i-1}^h \le x \le X_i^h, \\ \frac{X_{i+1}^h - x}{X_{i+1}^h - X_i^h}, & \text{if } X_i^h \le x \le X_{i+1}^h \le X_{N_x}^h, \\ 0, & \text{otherwise.} \end{cases} \tag{24}$$

$w_j^h(y)$ and $w_k^h(z)$ are similarly defined. Then $\frac{\delta\beta(\boldsymbol{x})}{\beta(\boldsymbol{x})}$ can be discretized on a multiple-grid as:

$$\frac{\delta\beta(\boldsymbol{x})}{\beta(\boldsymbol{x})} = \frac{1}{H}\sum_{h=1}^{H}\sum_{l=1}^{L_h}\delta C_l^h B_l^h(\boldsymbol{x}), \tag{25}$$

where δC_l^h is the discretized relative shear wave velocity perturbation at the lth grid node of the hth inversion grid, and L_h denotes the number of nodes of the hth inversion grid. Substituting Equation 25 in Equation 21, we have:

$$\frac{\partial\chi}{\partial C_l^h} = \frac{1}{H}\int_\Omega K_c^{\beta;\alpha,\rho}(\boldsymbol{x})B_l^h(\boldsymbol{x})d\boldsymbol{x}. \tag{26}$$

With the gradient provided in Equation 26, we can find an optimal vector $(C_1^1, \cdots, C_{L_1}^1, C_1^2, \cdots, C_{L_2}^2, \cdots, C_1^H, \cdots, C_{L_H}^H)$ that minimizes the objective function χ, using an optimization algorithm such as the gradient descent method. One way to do this is to employ the step-size-controlled gradient descent method discussed in Tong (2021a), which not only updates the model in the right direction but also plays a role similar to damping regularization in solving ill-posed problems.

The workflow of adjoint-state surface wave traveltime tomography is summarized as follows:

1. Generate the corresponding P-wave velocity model $\alpha(\boldsymbol{x})$ and density model $\rho(\boldsymbol{x})$ from a given shear wave velocity model $\beta(\boldsymbol{x})$, using empirical relationships (Equations S1 and S2 in Supporting Information S1).
2. Based on the 3D models of P-wave velocity, shear wave velocity, and density, determine the surface wave phase slowness $s_f(\boldsymbol{x^0})$ $(f \in \mathcal{F})$, assuming that the 3D model can be viewed as a layered model locally (Equation B11).
3. Apply a low-pass filter to the surface topography function, with the corner wavelength dependent on the surface wave wavelength.
4. Solve the eikonal equation (Equation 2) to obtain the traveltime field $T_{n,f}(\boldsymbol{x^0})$ for each frequency and source (virtual source).
5. Solve the adjoint equation (Equation 9) to obtain the adjoint field $P_{n,f}(\boldsymbol{x^0})$ for each frequency and source (virtual source).
6. Calculate the integrated shear wave velocity kernel (Equation 21).
7. Update the shear wave velocity model.
8. Repeat the iterative process from step 1 until either the maximum number of iterations is reached or the misfit function value falls below a predefined threshold value.

3. Application in Hawaii

To evaluate the performance of our newly developed method in real-world applications, we apply it to construct a shear wave velocity (Vs) model for the upper and middle crust beneath Hawaii Island (Figure 3).

3.1. Data and Inversion

The application of the adjoint-state surface wave traveltime tomography method to ambient noise surface wave data involves three main steps. First, Empirical Green's Functions (EGFs) are extracted from continuous ambient noise recordings. Second, surface wave phase traveltimes are measured on the EGFs. Third, we invert the surface wave phase traveltimes to construct a 3D Vs model.

The continuous ambient noise data used in this study are obtained from the HV, PT, and IU permanent seismic networks (Figure 3). We use continuous recordings from 5 September 2018 to 31 December 2018, a thoughtfully chosen period after the 2018 lower Puna eruption, to avoid the disruptions caused by ongoing volcanic activities

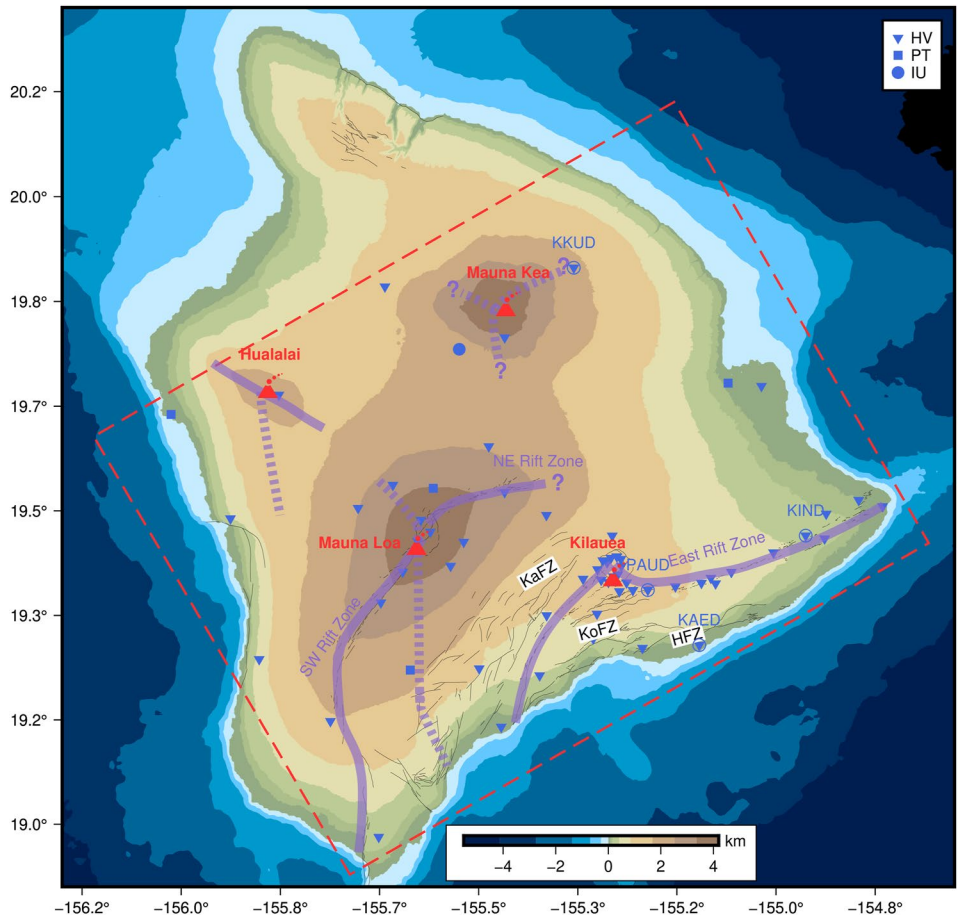

Figure 3. Geology map of Hawaii Island. The red triangles represent the major volcanoes, and the black lines denote the faults (Styron & Pagani, 2020). The solid and dashed purple lines mark the surficial and buried rift zones, respectively (Park et al., 2009; Wei et al., 2023). Question marks indicate the unknown extent of rift zones (Park et al., 2009). The red dashed rectangle outlines the research region. The blue inverted triangles, squares and solid circles denote seismic stations from the HV, PT and IU seismic networks, respectively. KKUD, KAED, PAUD and KIND are station names, with their locations indicated by the blue open circles. KoFZ: Koa'e Fault Zone; KaFZ: Kao'iki Fault Zone; HFZ: Hilina Fault Zone.

(Wei & Shen, 2022). The data processing mainly follows the procedures proposed by Bensen et al. (2007). The mean, trend and instrument response are removed. The waveform data are downsampled to 10 Hz before undergoing smoothing using the running-mean average method in both time and frequency domains. Cross correlation is performed on 3-hr segments with 1.5-hr overlapping, and the RMS-ratio selection stacking method is applied to improve the quality of the EGFs (Xie et al., 2020). A portion of the resulting EGFs are displayed in Figure 4b. Rayleigh wave phase traveltimes are measured on the EGFs. We measure the Rayleigh wave phase velocity dispersion curves within the period range from 2.5 to 9.5 s (Figure 4a) and calculate traveltimes based on these phase velocities. The inter-station distance is required to be longer than twice the surface wave wavelength for each frequency, and the phase velocities are picked on narrow-bandpass filtered waveforms (Yao et al., 2006). Two additional steps are taken to enhance the fundamental mode Rayleigh wave signals before narrow-bandpass filtering. First, a low-pass filter is applied to mitigate the disturbance of higher mode Rayleigh waves, which typically have higher frequencies at similar velocities. Second, a time window is applied to suppress the signals other than fundamental mode Rayleigh waves. The time window is selected based on the average group velocity dispersion curve of the fundamental mode Rayleigh wave, with a width of 5 times the central period of the narrow-bandpass filter (Wei et al., 2023). Examples of phase velocity picking are displayed in Figures S1–S3 in Supporting Information S1.

A 1D inversion is conducted to fit all observed dispersion curves, resulting in a horizontally homogeneous Vs model (Figure 4c). This model serves as the initial model for the 3D tomographic inversion. The Vs model is

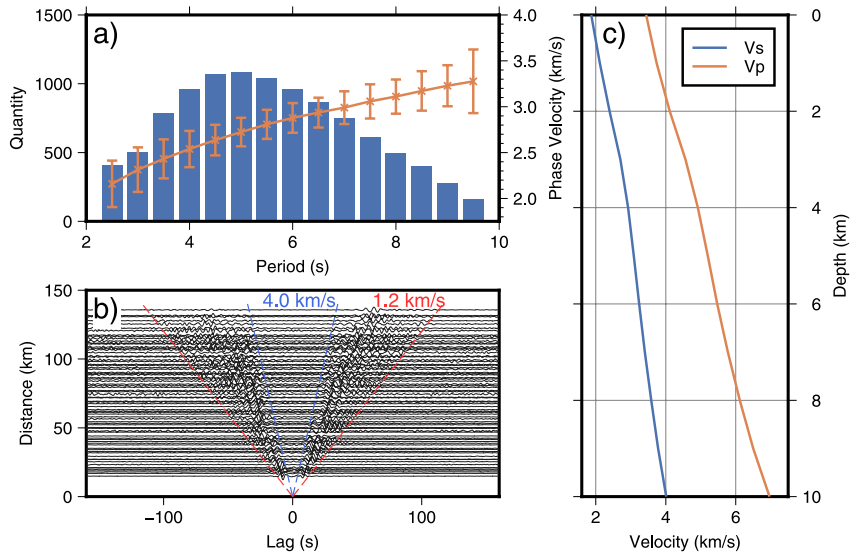

Figure 4. (a) Dispersion curves and their quantities. The orange line denotes the average dispersion curve and corresponding standard deviations, the blue bars denote the quantity of dispersion curves at each period. (b) Cross correlation functions, band-pass filtered between periods of 2.5–10 s. Only one waveform is displayed in each 1.5 km bin. (c) Initial velocity models.

discretized on a fine grid with dimensions of $1.0 \times 1.0 \times 1.0$ km. The inversion grid, on which the Vs perturbation is interpolated, consists of 5 sets of coarse regular grids (as showed in Figure S4 in Supporting Information S1). The final model presented here is obtained after 40 iterations starting from the initial model. In each iteration, the relative Vs perturbation is regulated by multiplying it by a factor such that the maximum relative Vs perturbation does not exceed a predefined cap value. This cap value is initially set at 2% and can be adjusted after each iteration. Specifically, if the misfit function does not decrease, the cap value of the relative Vs perturbation will be reduced to 90% of its preceding value.

3.2. Checkerboard Resolution Test

The checkerboard resolution test is implemented to assess the resolution of the obtained Vs model. First, we define a target Vs model with alternating high and low-velocity anomalies, with the perturbation expressed as:

$$\frac{\beta_{ckbd} - \beta_0}{\beta_0} = \begin{cases} 0.08 \sin\left(\frac{2\pi x}{59}\right) \sin\left(\frac{2\pi y}{60}\right) \sin\left(\frac{2\pi z}{10}\right) & z < 5.0, \\ 0.08 \sin\left(\frac{2\pi x}{79}\right) \sin\left(\frac{2\pi y}{60}\right) \sin\left(\frac{2\pi z}{10}\right) & z > 5.0, \end{cases} \tag{27}$$

where β_{ckbd} represents the target Vs model (Figure S5 in Supporting Information S1), and β_0 is the layered initial model (Figure 4c). We calculate Vp and density from Vs using empirical relationships (Equations S1 and S2 in Supporting Information S1). Next, we calculate synthetic Rayleigh wave phase traveltimes in the target model. To simulate the noise and picking errors in real data, the synthetic traveltimes are polluted by Gaussian noise, with a mean of 0 and a standard deviation of 0.1 s. Finally, we invert the synthetic traveltimes using the adjoint-state surface wave traveltime tomography method. Note that the initial model and inversion parameters are identical to those used in the real data inversion. The results of the checkerboard resolution test are shown in Figure 5, with most of the velocity anomalies being well recovered. However, the anomalies are poorly recovered in the northeast corner and at greater depth (>6 km) in the northwest corner, reflecting the lack of stations in these regions. Additional checkerboard tests are conducted with varying checker shapes (Figure S6 in Supporting Information S1) and smaller checker sizes (Figure S7 in Supporting Information S1), showing consistent resolution in areas comparable to those shown in Figure 5.

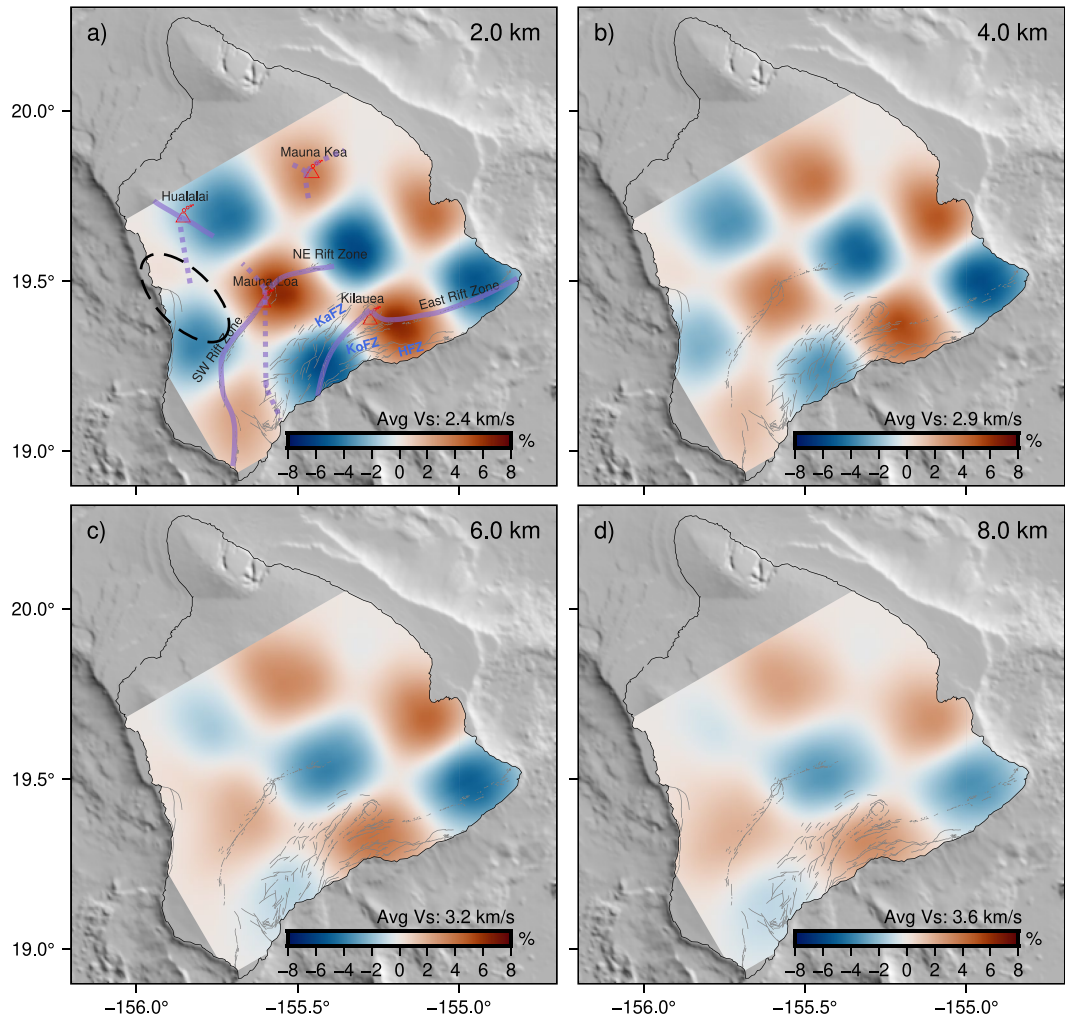

Figure 5. The results of checkerboard resolution test at depths of 2, 4, 6, 8 km, respectively. The depth is defined as the distance beneath the ground surface. Colors denote the relative shear wave velocity perturbation with respect to the initial model. The black dashed ellipse indicates a high-velocity anomaly in Figure 6. The input model is shown in Figure S5 in Supporting Information S1.

3.3. Tomographic Results

Figure 6 shows the horizontal slices of the optimal Vs model, which reveals velocity anomalies that are well consistent with the surface geological features. In detail, the model exhibits high Vs values beneath Mauna Loa Volcano, Kilauea Volcano and the southwestern flank of Mauna Kea Volcano, while low Vs values are observed beneath the Hilina Fault Zones. The Koa'e Fault Zone and the Kao'iki Fault Zone are located at the boundaries of a high Vs anomaly related to Kilauea Volcano. These results are generally in agreement with those of previous body wave tomography studies (e.g., G. Lin et al., 2014; Park et al., 2009). However, the resolution of body wave tomography is limited to the north of Mauna Loa Volcano due to low seismicity and sparse stations.

Compared with previous ambient noise surface wave tomography results in this region, our model shows similar features in the south of the research area (Miller, 2022; Wei et al., 2023). Discrepancy emerges near Hualalai's summit and Mauna Kea's summit, where the models of both this study and Miller (2022) show high-velocity anomalies, while the model of Wei et al. (2023) exhibits an average-to-low-velocity structure. Considering these velocity anomalies are poorly constrained by seismic data due to few seismic stations around the two summits (Figure 3), they should be interpreted cautiously.

The surface wave tomographic results enable us to delineate subsurface structures in the Island of Hawaii, which was formed as a result of volcanic activity (Moore & Clague, 1992). Intrusive structures, such as magma

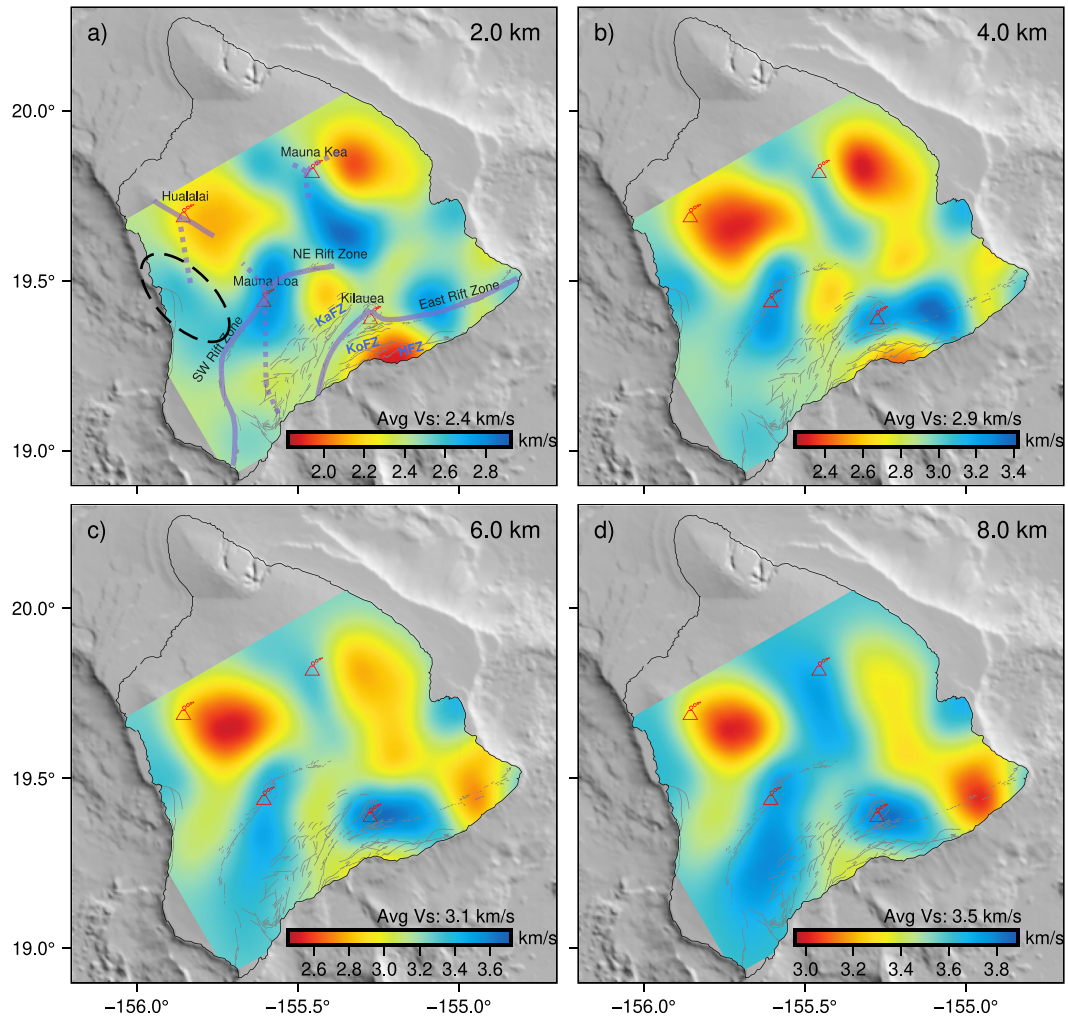

Figure 6. The resulting shear wave velocity model at depths of 2, 4, 6, 8 km, respectively. The depth is defined as the distance beneath the ground surface. The black dashed ellipse indicates a high-velocity anomaly.

cumulates and dike complexes are usually characterized by high velocities, while extrusive rocks usually exhibit low velocities (Flinders et al., 2013; Haslinger et al., 2001; Okubo et al., 1997; Park et al., 2009). Thus, the high-velocity anomalies may suggest the presence of buried rift zones, which are related to intrusive igneous rocks (Okubo et al., 1997). High Vs values are observed beneath Mauna Loa Volcano, and these anomalies broaden with depth while extending southwestward. These high Vs anomalies can be attributed to the magma cumulates and intrusive complexes beneath Mauna Loa's summit and in the Southwest Rift Zone. Our model also displays the existence of a high Vs anomaly beneath Mauna Kea Volcano, but the shape of the anomaly may not be well constrained as the data coverage in this area is insufficient (Figure 3). A high-velocity anomaly is observed to the east of Kilauea's summit, following the strike of the East Rift Zone. This eastward-extending high-velocity anomaly is interrupted by a low-velocity anomaly near the southeast corner of Hawaii Island, a feature also present in the Vp model from body wave tomography (Park et al., 2007, 2009). Additional data coverage and analysis may shed more light on the high Vs anomaly at the lower East Rift Zone and its separation from the upper East Rift Zone. High Bouguer gravity anomalies are observed at Mauna Loa's summit, Mauna Kea's summit, Kilauea's summit, East Rift Zone of Kilauea Volcano, and Southwest Rift Zone of Mauna Loa Volcano (>300 mGal), while moderate Bouguer gravity anomalies are present at Hualalai Volcano (250–300 mGal) (Flinders et al., 2013). The distributions and shapes of high Vs anomalies are mostly similar to those of high Bouguer gravity anomalies (Kauahikaua et al., 2000), consistent with the notion that high-velocity structures generally have high density (Brocher, 2005).

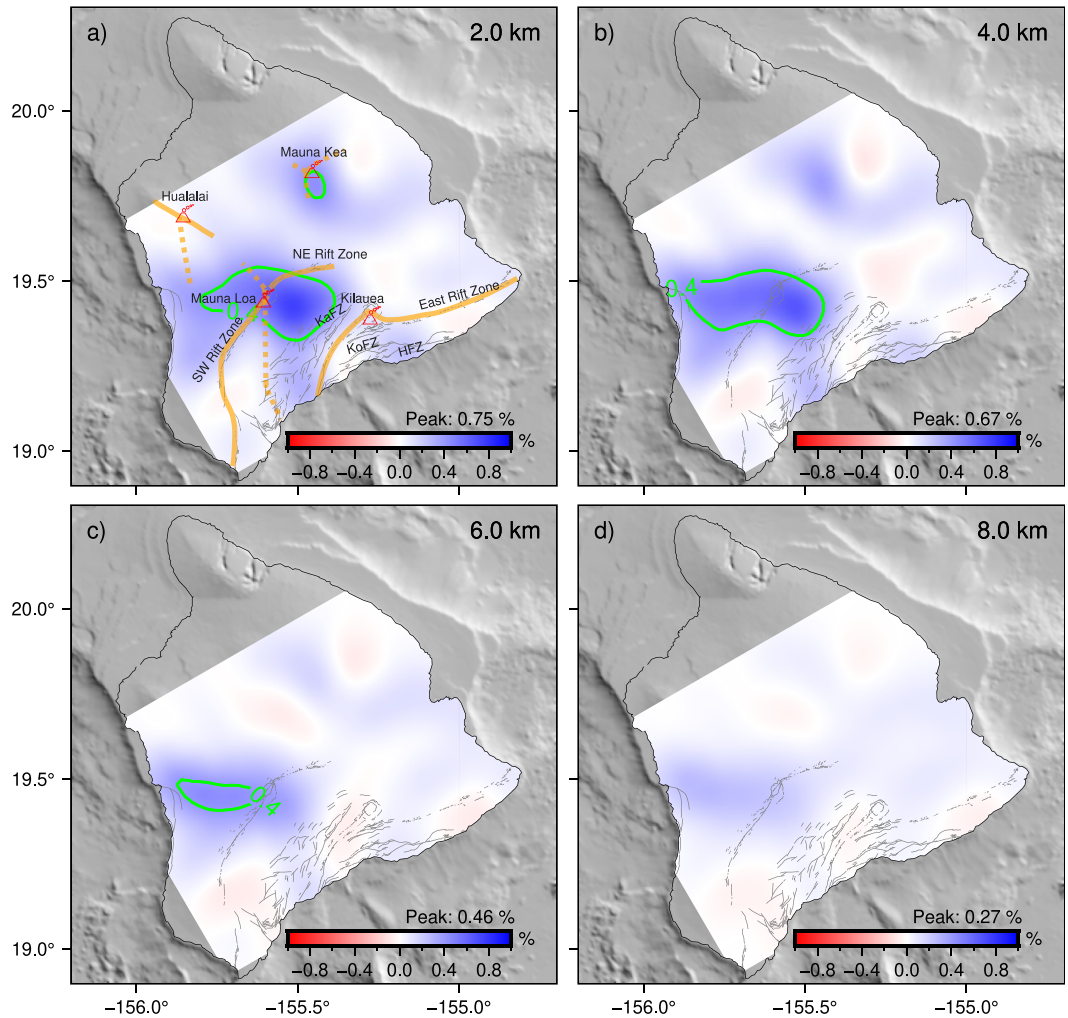

Figure 7. Estimation of shear wave velocity bias induced by ignoring the topographic variation. The bias is defined as the relative difference between Vs models from tomographic inversions incorporating (Figure 6) and ignoring topography (Figure S8 in Supporting Information S1). The green lines delineate contours of 0.4%. The maximum value of the relative Vs difference is indicated above the color bar. The depth is defined as the distance beneath the ground surface.

Furthermore, there is a high-velocity anomaly to the south of Hualalai's summit (Figure 6a). As inferred from the high Bouguer gravity anomalies and long-wavelength linear magnetic low zones (Flinders et al., 2013; Hildenbrand et al., 1993; Kauahikaua et al., 2000), the presence of a buried rift zone to the south of Hualalai's summit has been suggested by previous studies. Park et al. (2009) reported increased Vp to the south of Hualalai's summit, while the resolution is limited by the sparse stations. Moreover, a seismic refraction profile crossing the south of Hualalai's summit suggests a high Vp anomaly (Zucca et al., 1982). The high Vs presented to the south of Hualalai's summit may also be related to this buried rift zone.

Our new surface wave tomography method has the capability of improving the accuracy of tomographic inversions by explicitly addressing topographic variations. Overlooking the deviation of the propagation path from the horizontal plane can lead to an underestimation of the propagation distance given a specific traveltime observation, which in turn can generate apparent velocity anomalies. This phenomenon can be referred to as the distance effect. To assess the impact of distance effect, we perform an additional inversion using the same data and parameters but disregarding the topography. Neglecting the topography leads to an underestimation of the interstation distance, which can potentially introduce low-velocity artifacts. Figure 7 illustrates the relative difference in the shear wave velocity obtained from tomographic inversions incorporating and ignoring topography. The results reveal that ignoring topography generally leads to an underestimation of velocity, particularly beneath Mauna Loa Volcano. The difference in Vs can reach up to 0.023 km/s (0.8%). However, when examining Hawaii Island

and using Rayleigh waves with dominant periods from 2.5 to 9.5 s, the patterns of the Vs anomalies are similar, regardless of whether the topography is taken into account or not (Figure S8 in Supporting Information S1). The amplitude of the Vs model correction is comparable to the amplitude of traveltime biases calculated by Miller (2022).

4. Discussion and Conclusions

We have developed a novel surface wave traveltime tomography method that accounts for both topography variations and velocity heterogeneities. Our approach involves minimizing the misfit between the observed and calculated surface wave traveltimes to obtain an optimal shear wave velocity model. We utilize an elliptically anisotropic eikonal equation to simulate surface wave traveltime fields on undulated topography (see Equation 2). By using the efficient adjoint-state method, we derive the sensitivity kernel of the misfit function with respect to shear wave velocity, which allows us to directly invert for shear wave velocity without constructing a surface wave phase velocity map. Additionally, we leverage empirical relationships between Vp and Vs, as well as between density and Vs, to reduce the number of unknowns in the tomographic inversion.

Equation 2 is employed to model surface wave propagation along a curved surface. However, there may be concerns about the ability of the eikonal equation to accurately simulate wave propagation in complex media, including the scattering effects caused by topographic variations. Several previous studies have shown that the distance effect plays a significant role in the topography-induced errors. For example, Köhler et al. (2012) used the spectral element method to simulate seismograms (period 3–5 s) in a model with topographic variation and found that the distance effect can effectively correct the topography-induced error when the topography gradient near the seismic receiver is small. Similarly, Ning et al. (2018) simulated seismograms using the finite-difference method and demonstrated that using distance all along the curved surface can significantly reduce the topography-induced error. Therefore, calculating surface wave traveltimes along a curved surface is an effective approach to simulate the influence of topography.

We have successfully implemented our method on the Island of Hawaii, where the volcanic topography can introduce inaccuracy to surface wave tomography approaches ignoring surface topography. Our tomographic results exhibit good consistency with known geologic structures and previous tomographic models (e.g., G. Lin et al., 2014; Okubo et al., 1997; Park et al., 2009; Wei et al., 2023; Miller, 2022). The obtained Vs model extends into regions where body wave tomography has limited resolution due to low seismicity and sparse stations. Specifically, our results reveal a high-velocity anomaly to the south of Hualalai's summit, which may be related to the presence of a buried rift zone.

The incorporation of topography can introduce a correction to the amplitude of velocity anomalies in Hawaii, while the overall patterns remain consistent. These findings suggest that, in ambient noise surface wave tomography (using data with periods >2 s), ignoring topography in the Island of Hawaii and similar regions with comparable variations is a reasonable assumption. However, the assessment and correction of topographic influence become more crucial on smaller scales, where topographic variations can be more significant (e.g., Pilz et al., 2013). A checkerboard test was conducted on real-world topography measured on the campus of Nanyang Technological University (Figures S9–S11 in Supporting Information S1), revealing strong artifacts when topography is entirely disregarded.

One advantage of traveltime tomography is its computational efficiency. In our application to Hawaii Island, the Vs model is obtained after 40 iterations, taking a total of 40 min, utilizing 40 CPU cores (AMD EPYC 7713 up to 3.6 GHz). Compared with a typical wave equation-based tomography method (e.g., K. Wang et al., 2018), which usually takes days of computation, our method displays much higher efficiency. The storage space requirement of the adjoint-state traveltime tomography method mainly depends on the grid size.

Furthermore, the influence of topography is particularly worth considering in azimuthally anisotropic tomography. Actually, the 2D eikonal equation used in our approach to describe surface wave traveltime fileds on undulated topography has a similar form as the eikonal equation used to model traveltime fields in azimuthally anisotropic media (Tong, 2021b), which may indicate that the topographic parameters and azimuthally anisotropic parameters are coupled to a certain extent in surface wave traveltime tomography. Therefore, ignoring topography effect when inverting for azimuthally anisotropic velocity may introduce apparent anisotropy related to topographic variations. In future work, we will extend the present method to conduct surface wave azimuthal anisotropic tomography with topography in consideration.

In conclusion, the adjoint-state surface wave traveltime tomography method can effectively invert for shear wave velocity from surface wave traveltime measurements while also improving the accuracy by explicitly addressing surface topography.

Appendix A: Eikonal Equation on a Curved Surface

We consider surface waves propagate perfectly along a curved surface, defined as $z = \Phi(x, y)$. In this case, Equation 1 can no longer accurately describe the relationship between the traveltime gradient $\nabla T = \left(\frac{\partial T}{\partial x}, \frac{\partial T}{\partial y}, 0\right)$ and slowness s_f. We can derive an eikonal equation on a curved surface by replacing ∇T with the gradient along the curved surface, which can be obtained by projecting ∇T in the tangent direction of the surface (Tsai et al., 2003). It can be readily demonstrated that the vector $\boldsymbol{n} = (\Phi_x, \Phi_y, 1)$ is normal to the curved surface. Define operator:

$$O_{\parallel} = I - \frac{\boldsymbol{n}\boldsymbol{n}^t}{\|\boldsymbol{n}\|^2}. \tag{A1}$$

We can project ∇T on the tangent direction of the topography by multiplying $O_{\parallel}$. As a result,the eikonal equation with topography can be written as:

$$\left[\nabla T_{n,f}(\boldsymbol{x})\right]^t O_{\parallel}^t O_{\parallel} \nabla T_{n,f}(\boldsymbol{x}) = s_f^2(\boldsymbol{x}). \tag{A2}$$

Substitute Equation A1 into Equation A2:

$$\left[\nabla T_{n,f}(\boldsymbol{x})\right]^t \frac{1}{\Phi_x^2 + \Phi_y^2 + 1} \begin{bmatrix} 1+\Phi_y^2 & -\Phi_x\Phi_y & \Phi_x \\ -\Phi_x\Phi_y & 1+\Phi_x^2 & \Phi_y \\ \Phi_x & \Phi_y & \Phi_x^2+\Phi_y^2 \end{bmatrix} \nabla T_{n,f}(\boldsymbol{x}) = s_f^2(\boldsymbol{x}). \tag{A3}$$

It is important to note that $\nabla T_{n,f} = \left(\frac{\partial T_{n,f}}{\partial x}, \frac{\partial T_{n,f}}{\partial y}, 0\right)$. Hence, Equation A3 is equivalent to Equation 2. The physical interpretation of Equation 2 can be elucidated through its integration form (Kao et al., 2005):

$$T_{n,f}(\boldsymbol{x}_{r,m}) = \min_{\gamma \subset S} \int_{\gamma} s_f(\boldsymbol{x}) d\boldsymbol{x}, \tag{A4}$$

where $T_{n,f}$ is the solution of Equation 2, γ is an arbitrary curve that connects source $\boldsymbol{x}_{s,n}$ and receiver $\boldsymbol{x}_{r,m}$ on the curved surface S, S is defined as $z = \Phi(x, y)$.

Appendix B: Rayleigh Wave Phase and Group Velocities

The surface wave propagating along the direction of increasing x can be written as (Aki & Richards, 2002):

$$\boldsymbol{u}(x, y, z, t) = \boldsymbol{Z}(z) e^{i(kx - \omega t)}, \tag{B1}$$

where k is the wave number, ω is the frequency. Consider an isotropic, horizontally homogeneous velocity model with N layers, where α_n, β_n, ρ_n are P wave velocity, S wave velocity and density in the nth layer:

$$\begin{cases} \alpha_1, \beta_1, \rho_1 & 0 < z < z_1, \\ \cdots & \\ \alpha_n, \beta_n, \rho_n & z_{n-1} < z < z_n, \\ \cdots & \\ \alpha_N, \beta_N, \rho_N & z_{N-1} < z. \end{cases} \tag{B2}$$

Based on the elastic wave equation for isotropic media (Aki & Richards, 2002), the displacement in the nth layer satisfies:

$$\begin{cases} \rho_n \frac{\partial^2 u_x}{\partial t^2} = (\lambda_n + 2\mu_n)\frac{\partial^2 u_x}{\partial x^2} + (\lambda_n + \mu_n)\frac{\partial^2 u_z}{\partial z \partial x} + \mu_n \frac{\partial^2 u_x}{\partial z^2}, \\ \rho_n \frac{\partial^2 u_z}{\partial t^2} = (\lambda_n + 2\mu_n)\frac{\partial^2 u_z}{\partial z^2} + (\lambda_n + \mu_n)\frac{\partial^2 u_x}{\partial z \partial x} + \mu_n \frac{\partial^2 u_z}{\partial x^2}, \\ \rho_n \frac{\partial^2 u_y}{\partial t^2} = \mu_n \left(\frac{\partial^2 u_y}{\partial x^2} + \frac{\partial^2 u_y}{\partial z^2} \right), \end{cases} \tag{B3}$$

where μ_n, λ_n are elastic parameters with $\alpha_n = \sqrt{\frac{\lambda_n + 2\mu_n}{\rho_n}}$, $\beta_n = \sqrt{\frac{\mu_n}{\rho_n}}$. Equation B3 shows that the displacement in the $x - z$ plane is independent of the displacement in the y direction. The third equation in Equation B3 describes the displacement of Love waves. The calculation method for Love wave dispersion curves is derived in detail in Aki and Richards (2002). Here we derive Rayleigh wave velocities following a similar manner. We can write Rayleigh wave displacement as (u_x, 0, u_z) and use the following trial solution:

$$\begin{cases} u_x(x, z, t) = U(z) e^{i(kx - \omega t)}, \\ u_z(x, z, t) = V(z) e^{i(kx - \omega t)}. \end{cases} \tag{B4}$$

Substitute Equation B4 into Equation B3:

$$\begin{cases} \left[\omega^2 \rho_n - k^2(\lambda_n + 2\mu_n)\right] U + ik(\lambda_n + \mu_n) V' + \mu_n U'' = 0, \\ \left[\omega^2 \rho_n - k^2 \mu_n\right] V + ik(\lambda_n + \mu_n) U' + (\lambda_n + 2\mu_n) V'' = 0. \end{cases} \tag{B5}$$

The solutions are:

$$\begin{cases} U(z) = A_n e^{a_n z} + B_n e^{-a_n z} + C_n e^{b_n z} + D_n e^{-b_n z}, \\ V(z) = -\frac{ia}{k} A_n e^{a_n z} + \frac{ia}{k} B_n e^{-a_n z} - \frac{ik}{b} C_n e^{b_n z} + \frac{ik}{b} D_n e^{-b_n z}, \end{cases} \tag{B6}$$

where A_n, B_n, C_n, D_n are unknown constants, $a_n = \sqrt{k^2 - \frac{\omega^2}{\alpha_n^2}}$, $b_n = \sqrt{k^2 - \frac{\omega^2}{\beta_n^2}}$. Enforce the following boundary conditions:

1. When $z = 0$, implementing the free surface boundary condition by setting $\tau_{xz} = \tau_{zz} = 0$.
2. When $z = z_n$, u_x, u_z, τ_{xz}, τ_{zz} are continuous.
3. When $z \to \infty$, the amplitude of Rayleigh wave equals to zero. Assume that z_{N-1} is large enough so that the surface wave energy has completely decayed at that depth. To ensure this condition, we have $A_N = C_N = 0$, $k^2 - \frac{\omega^2}{\alpha_N^2} > 0$, $k^2 - \frac{\omega^2}{\beta_N^2} > 0$.

Substitute the solutions u_x, u_z into the free surface conditions at $z = 0$:

$$\begin{cases} 2a_1 A_1 - 2a_1 B_1 + \left(b_1 + \frac{k^2}{b_1}\right) C_1 - \left(b_1 + \frac{k^2}{b_1}\right) D_1 = 0, \\ \left(k^2 + b_1^2\right) A_1 + \left(k^2 + b_1^2\right) B_1 + 2k^2 C_1 + 2k^2 D1 = 0. \end{cases} \tag{B7}$$

Substitute the solutions u_x, u_z into the continuous conditions between the nth and the $(n + 1)$-th layer (n = 1, 2, …, $N - 1$):

$$\begin{cases} U_n - U_{n+1} = 0, \\ V_n - V_{n+1} = 0, \\ \mu_n(U_n' + ikV_n) - \mu_{n+1}\left(U_{n+1}' + ikV_{n+1}\right) = 0, \\ (\lambda_n + 2\mu_n)V_n' + ik\lambda_n U_n - (\lambda_{n+1} + 2\mu_{n+1})V_{n+1}' - ik\lambda_{n+1}U_{n+1} = 0, \end{cases} \tag{B8}$$

where:

$$\begin{cases} U_n = e^{a_n z_n}A_n + e^{-a_n z_n}B_n + e^{b_n z_n}C_n + e^{-b_n z_n}D_n, \\ U_n' = a_n e^{a_n z_n}A_n - a_n e^{-a_n z_n}B_n + b_n e^{b_n z_n}C_n - b_n e^{-b_n z_n}D_n, \\ V_n = -\frac{ia_n}{k}e^{a_n z_n}A_n + \frac{ia_n}{k}e^{-a_n z_n}B_n - \frac{ik}{b_n}e^{b_n z_n}C_n + \frac{ik}{b_n}e^{-b_n z_n}D_n, \\ V_n' = -\frac{ia_n^2}{k}e^{a_n z_n}A_n - \frac{ia_n^2}{k}e^{-a_n z_n}B_n - ike^{b_n z_n}C_n - ike^{-b_n z_n}D_n. \end{cases} \tag{B9}$$

$U_{n+1}, V_{n+1}, U_{n+1}', V_{n+1}'$ are similarly defined. Equations B7 and B8 form a homogeneous system of linear equations, consisting of 4N − 2 equations in 4N − 2 variables. It can be written in matrix form:

$$\boldsymbol{Gm} = \boldsymbol{0}, \tag{B10}$$

where $\boldsymbol{m} = (A_1, \ldots, A_{N-1}, B_1, \ldots, B_N, C_1, \ldots, C_{N-1}, D_1, \ldots, D_N)$, $\boldsymbol{G}$ is composed of model parameters α_n, β_n, ρ_n, z_n and k, ω. A non-trivial solution only exists when:

$$\det(\boldsymbol{G}) = g(k, \omega; \alpha_n, \beta_n, \rho_n, z_n) = 0. \tag{B11}$$

By solving Equation B11, we can obtain the relationship between k and ω. Rayleigh wave phase velocity can be calculated by $c = \frac{\omega}{k}$, while group velocity can be calculated by $c = \frac{d\omega}{dk}$.

Appendix C: Rayleigh Wave Sensitivity Kernels

Surface wave velocity kernels are the partial derivatives of the phase or group velocity with respect to the body wave velocity and density. With the ability of calculating surface wave velocity from a given body wave velocity and density model, the kernels can be calculated using finite difference method. The surface wave kernels can also be derived by variational principle (Aki & Richards, 2002), which is more computationally efficient. Continuing from the derivation presented by Aki and Richards (2002) on surface wave velocity kernels with respect to elastic modulus, this Appendix further derive surface wave velocity kernels with respect to body wave velocities, for the completeness of the method discussed in the main text.

Assume that the Lamé parameters $\lambda(z)$ and $\mu(z)$ and the density $\rho(z)$ are functions of z. We write Rayleigh wave displacement as:

$$\begin{cases} u_x(x, z, t) = r_1(z)e^{i(kx-\omega t)}, \\ u_z(x, z, t) = ir_2(z)e^{i(kx-\omega t)}. \end{cases} \tag{C1}$$

Based on the Hooke's law, the stresses are:

$$\begin{cases} \tau_{xx}(x, z, t) = i\left[\lambda\frac{dr_2}{dz} + k(\lambda + 2\mu)r_1\right]e^{i(kx-\omega t)}, \\ \tau_{xz}(x, z, t) = \mu\left(\frac{dr_1}{dz} - kr_2\right)e^{i(kx-\omega t)}, \\ \tau_{zz}(x, z, t) = i\left[(\lambda + 2\mu)\frac{dr_2}{dz} + k\lambda r_1\right]e^{i(kx-\omega t)}. \end{cases} \tag{C2}$$

To avoid involving second order derivatives of r_1 and r_2, we can rewrite the stresses as:

$$\begin{cases} \tau_{xx}(x,z,t) = \frac{i}{\lambda+2\mu}[\lambda r_4 + 4k\mu(\lambda+\mu)r_1]e^{i(kx-\omega t)}, \\ \tau_{xz}(x,z,t) = r_3 e^{i(kx-\omega t)}, \\ \tau_{zz}(x,z,t) = i r_4 e^{i(kx-\omega t)}, \end{cases} \tag{C3}$$

where

$$\begin{cases} r_3 = \mu\left(\frac{dr_1}{dz} - kr_2\right), \\ r_4 = (\lambda+2\mu)\frac{dr_2}{dz} + k\lambda r_1. \end{cases} \tag{C4}$$

Consequently, the wave equation for Rayleigh waves becomes:

$$\begin{cases} \frac{dr_3}{dz} = \left[k^2\frac{4\mu(\lambda+\mu)}{\lambda+2\mu} - \omega^2\rho\right]r_1 + \frac{k\lambda}{\lambda+2\mu}r_4, & \text{(C5a)} \\ \frac{dr_4}{dz} = -\omega^2\rho r_2 - kr_3. & \text{(C5b)} \end{cases}$$

Equations (C4) and (C5) constitute an eigenvalue problem, with the boundary conditions being $r_3 = r_4 = 0$ at $z = 0$, and $r_1 \to 0$, $r_2 \to 0$ as $z \to \infty$. The eigenfunctions r_1, r_2, r_3, r_4 can be solved by numerical methods such as the numerical integration method or the propagator matrix method (Aki & Richards, 2002). The Rayleigh wave sensitivity kernels can then be derived as expressions of r_1 and r_2. Define:

$$\begin{cases} I_1 = \frac{1}{2}\int_0^\infty \rho\left(r_1^2 + r_2^2\right)dz, \\ I_2 = \frac{1}{2}\int_0^\infty \left[(\lambda+2\mu)r_1^2 + \mu r_2^2\right]dz, \\ I_3 = \int_0^\infty \left(\lambda r_1\frac{dr_2}{dz} - \mu r_2\frac{dr_1}{dz}\right)dz, \\ I_4 = \frac{1}{2}\int_0^\infty \left[(\lambda+2\mu)\left(\frac{dr_2}{dz}\right)^2 + \mu\left(\frac{dr_1}{dz}\right)^2\right]dz. \end{cases} \tag{C6}$$

For linear elastic materials, the Lagrangian density is defined as the difference between the kinetic energy and the elastic strain energy. Based on this definition, $\omega^2 I_1 - k^2 I_2 - kI_3 - I_4$ is the integral of the Lagrangian density for the Rayleigh wave described by Equations (C4) and (C5). To derive the value of this Lagrangian density integral, we make use of Equations (C4) and (C5). Specifically, we substitute Equation C4 in Equation (C5). Then, Equation (C5a) is multiplied by r_1 and integrated over z. Similarly, Equation (C5b) is multiplied by r_2 and integrated over z:

$$\begin{cases} \int_0^\infty \left[\omega^2\rho - k^2(\lambda+2\mu)\right]r_1^2 dz + \int_0^\infty k\mu\frac{dr_1}{dz}r_2 dz - \int_0^\infty k\lambda\frac{dr_2}{dz}r_1 dz - \int_0^\infty \mu\left(\frac{dr_1}{dz}\right)^2 dz = 0, \\ \int_0^\infty \left[\omega^2\rho - k^2\mu\right]r_2^2 dz + \int_0^\infty k\mu\frac{dr_1}{dz}r_2 dz - \int_0^\infty k\lambda\frac{dr_2}{dz}r_1 dz - \int_0^\infty (\lambda+2\mu)\left(\frac{dr_2}{dz}\right)^2 dz = 0. \end{cases} \tag{C7}$$

Adding two equations in Equation C7, it can be observed that:

$$\omega^2 I_1 - k^2 I_2 - kI_3 - I_4 = 0. \tag{C8}$$

Furthermore, based on Hamilton's principle (Aki & Richards, 2002), the Lagrangian density integral is stationary under first-order perturbations of r_1 and r_2:

$$\omega^2\delta I_1 - k^2\delta I_2 - k\delta I_3 - \delta I_4 = 0, \tag{C9}$$

where δI_1, δI_2, δI_3, and δI_4 are perturbations with respect to r_1 and r_2. Substitute Equation C6 into Equation C9:

$$\begin{aligned}\frac{1}{2}\omega^2\int_0^\infty [2\rho(r_1\delta r_1 + r_2\delta r_2)]dz\\ -\frac{1}{2}k^2\int_0^\infty [(\lambda+2\mu)(2r_1\delta r_1)+\mu(2r_2\delta r_2)]dz\\ -k\int_0^\infty\left[\lambda r_1\frac{d(\delta r_2)}{dz}+\lambda\delta r_1\frac{dr_2}{dz}-\mu r_2\frac{d(\delta r_1)}{dz}-\mu\delta r_2\frac{dr_1}{dz}\right]dz\\ -\frac{1}{2}\int_0^\infty\left[2\frac{d(\delta r_2)}{dz}\frac{dr_2}{dz}(\lambda+2\mu)+2\mu\frac{d(\delta r_1)}{dz}\frac{dr_1}{dz}\right]dz=0.\end{aligned} \tag{C10}$$

For a given frequency ω, we can introduce perturbations to the density and elastic parameters $\rho+\delta\rho$, $\lambda+\delta\lambda$, $\mu+\delta\mu$. The corresponding wavenumber and eigenvalues become $k+\delta k$, $r_1+\delta r_1$, $r_2+\delta r_2$. These perturbed values also adhere to the relationship in Equation C8:

$$\begin{aligned}\frac{1}{2}\omega^2\int_0^\infty(\rho+\delta\rho)\left[(r_1+\delta r_1)^2+(r_2+\delta r_2)^2\right]dz\\ -\frac{1}{2}(k+\delta k)^2\int_0^\infty\left[(\lambda+\delta\lambda+2\mu+2\delta\mu)(r_1+\delta r_1)^2+(\mu+\delta\mu)(r_2+\delta r_2)^2\right]dz\\ -(k+\delta k)\int_0^\infty\left[(\lambda+\delta\lambda)(r_1+\delta r_1)\frac{d(r_2+\delta r_2)}{dz}-(\mu+\delta\mu)(r_2+\delta r_2)\frac{d(r_1+\delta r_1)}{dz}\right]dz\\ -\frac{1}{2}\int_0^\infty\left[(\lambda+\delta\lambda+2\mu+2\delta\mu)\left(\frac{d(r_2+\delta r_2)}{dz}\right)^2+(\mu+\delta\mu)\left(\frac{d(r_1+\delta r_1)}{dz}\right)^2\right]dz=0.\end{aligned} \tag{C11}$$

Subtracting the original Equation C8 from Equation C11, and only retaining the first-order terms, we have:

$$\begin{aligned}\frac{1}{2}\omega^2\int_0^\infty\left[\delta\rho\left(r_1^2+r_2^2\right)+2\rho(r_1\delta r_1+r_2\delta r_2)\right]dz\\ -k\delta k\int_0^\infty\left[(\lambda+2\mu)r_1^2+\mu r_2^2\right]dz\\ -\frac{1}{2}k^2\int_0^\infty\left[(\lambda+2\mu)(2r_1\delta r_1)+(\delta\lambda+2\delta\mu)r_1^2+\delta\mu r_2^2+\mu(2r_2\delta r_2)\right]dz\\ -\delta k\int_0^\infty\left(\lambda r_1\frac{dr_2}{dz}-\mu r_2\frac{dr_1}{dz}\right)dz\\ -k\int_0^\infty\left[\lambda r_1\frac{d(\delta r_2)}{dz}+\lambda\delta r_1\frac{dr_2}{dz}+\delta\lambda r_1\frac{dr_2}{dz}-\mu r_2\frac{d(\delta r_1)}{dz}-\mu\delta r_2\frac{dr_1}{dz}-\delta\mu r_2\frac{dr_1}{dz}\right]dz\\ -\frac{1}{2}\int_0^\infty\left[2\frac{d(\delta r_2)}{dz}\frac{dr_2}{dz}(\lambda+2\mu)+(\delta\lambda+2\delta\mu)\left(\frac{dr_2}{dz}\right)^2+\delta\mu\left(\frac{dr_1}{dz}\right)^2+2\mu\frac{d(\delta r_1)}{dz}\frac{dr_1}{dz}\right]dz=0.\end{aligned} \tag{C12}$$

By subtracting Equation C10 from Equation C12, we can write the relationship between δk and $\delta\rho$, $\delta\lambda$, $\delta\mu$:

$$\begin{aligned}\int_0^\infty\frac{1}{2}\omega^2\left(r_1^2+r_2^2\right)\delta\rho dz+\int_0^\infty-\frac{1}{2}\left(r_1k+\frac{dr_2}{dz}\right)^2\delta\lambda dz\\ +\int_0^\infty-\frac{1}{2}\left[\left(kr_2-\frac{dr_1}{dz}\right)^2+2k^2r_1^2+2\left(\frac{dr_2}{dz}\right)^2\right]\delta\mu dz=\delta k(2kI_2+I_3).\end{aligned} \tag{C13}$$

From Equation C13, we can express δk as an integral of the model perturbations $\delta\rho$, $\delta\lambda$, $\delta\mu$. Furthermore, the perturbation of the phase velocity c at a given frequency ω can be represented as a function of the perturbations in body wave velocities and density:

$$\delta c=-\frac{\omega}{k^2}\delta k=\int_0^\infty\left[K^\alpha_{c,\omega}\delta\alpha+K^\beta_{c,\omega}\delta\beta+K^\rho_{c,\omega}\delta\rho\right]dz, \tag{C14}$$

where:

$$\begin{cases} K^{\rho}_{c,\omega}(z) = -\frac{\omega}{k^2(2kI_2+I_3)}\left\{\frac{1}{2}\omega^2\left(r_1^2+r_2^2\right)-\frac{1}{2}\left(r_1k+\frac{dr_2}{dz}\right)^2\left(\alpha^2-2\beta^2\right)\right. \\ \qquad \left.-\frac{1}{2}\left[\left(kr_2-\frac{dr_1}{dz}\right)^2+2k^2r_1^2+2\left(\frac{dr_2}{dz}\right)^2\right]\beta^2\right\}, \\ K^{\alpha}_{c,\omega}(z) = \frac{\omega}{k^2(2kI_2+I_3)}\alpha\rho\left(r_1k+\frac{dr_2}{dz}\right)^2, \\ K^{\beta}_{c,\omega}(z) = -\frac{\omega}{k^2(2kI_2+I_3)}\left\{2\beta\rho\left(r_1k+\frac{dr_2}{dz}\right)^2-\beta\rho\left[\left(kr_2-\frac{dr_1}{dz}\right)^2+2k^2r_1^2+2\left(\frac{dr_2}{dz}\right)^2\right]\right\}. \end{cases} \tag{C15}$$

Data Availability Statement

All seismic data were downloaded through the IRIS Web Services (Trabant et al., 2012, https://service.iris.edu/), including the following seismic networks: (a) the HV (USGS Hawaiian Volcano Observatory (HVO), 1956); (b) the PT (Pacific Tsunami Warning Center, 1965); (c) the IU (Albuquerque Seismological Laboratory/USGS (ASL), United States of America, 2014). Version 6.4.0 of the Generic Mapping Tool used for making most figures is preserved at https://github.com/GenericMappingTools/gmt, available via GNU Lesser General Public License version 3 (Wessel et al., 2019).

Acknowledgments
This work is funded by Minister of Education, Singapore, under its MOE AcRF Tier-2 Grant (MOE-T2EP20122-0008) and its MOE AcRF Tier-1 Grant (RG86/22).

References

Aki, K., & Richards, P. G. (2002). Quantitative seismology.

Albuquerque Seismological Laboratory/USGS (ASL), United States of America. (2014). Global seismograph network (GSN—IRIS/USGS) (GSN) [Dataset]. International Federation of Digital Seismograph Networks. https://doi.org/10.7914/SN/IU

Barmin, M., Ritzwoller, M., & Levshin, A. (2001). A fast and reliable method for surface wave tomography. *Monitoring the comprehensive nuclear-test-ban treaty: Surface waves*, *158*(8), 1351–1375. https://doi.org/10.1007/pl00001225

Beaty, K. S., Schmitt, D. R., & Sacchi, M. (2002). Simulated annealing inversion of multimode Rayleigh wave dispersion curves for geological structure. *Geophysical Journal International*, *151*(2), 622–631. https://doi.org/10.1046/j.1365-246x.2002.01809.x

Bensen, G., Ritzwoller, M., Barmin, M., Levshin, A. L., Lin, F., Moschetti, M., et al. (2007). Processing seismic ambient noise data to obtain reliable broad-band surface wave dispersion measurements. *Geophysical Journal International*, *169*(3), 1239–1260. https://doi.org/10.1111/j.1365-246x.2007.03374.x

Borisov, D., Modrak, R., Gao, F., & Tromp, J. (2018). 3D elastic full-waveform inversion of surface waves in the presence of irregular topography using an envelope-based misfit function3d elastic FWI using envelopes. *Geophysics*, *83*(1), R1–R11. https://doi.org/10.1190/geo2017-0081.1

Brocher, T. M. (2005). Empirical relations between elastic wavespeeds and density in the Earth's crust. *Bulletin of the Seismological Society of America*, *95*(6), 2081–2092. https://doi.org/10.1785/0120050077

Castellanos, J. C., & Clayton, R. W. (2021). The fine-scale structure of Long Beach, California, and its impact on ground motion acceleration. *Journal of Geophysical Research: Solid Earth*, *126*(12), e2021JB022462. https://doi.org/10.1029/2021JB022462

Chen, J., Wu, S., Xu, M., Nagaso, M., Yao, J., Wang, K., et al. (2023). Adjoint-state teleseismic traveltime tomography: Method and application to Thailand in Indochina Peninsula. *Journal of Geophysical Research: Solid Earth*, *128*(12), e2023JB027348. https://doi.org/10.1029/2023JB027348

Cruz-Hernández, F., Gallardo, L. A., Calò, M., Castro, R. R., & Romo-Jones, J. M. (2022). Laterally constrained surface wave inversion. *Geophysical Journal International*, *230*(2), 1121–1131. https://doi.org/10.1093/gji/ggac108

Fang, H., Yao, H., Zhang, H., Huang, Y.-C., & van der Hilst, R. D. (2015). Direct inversion of surface wave dispersion for three-dimensional shallow crustal structure based on ray tracing: Methodology and application. *Geophysical Journal International*, *201*(3), 1251–1263. https://doi.org/10.1093/gji/ggv080

Fang, J., Yang, Y., Shen, Z., Biondi, E., Wang, X., Williams, E. F., et al. (2022). Directional sensitivity of DAS and its effect on Rayleigh-wave tomography: A case study in Oxnard, California. *Seismological Research Letters*, *94*(2A), 887–897. https://doi.org/10.1785/0220220235

Fichtner, A., Bunge, H.-P., & Igel, H. (2006). The adjoint method in seismology: I. Theory. *Physics of the Earth and Planetary Interiors*, *157*(1–2), 86–104. https://doi.org/10.1016/j.pepi.2006.03.016

Flinders, A. F., Ito, G., Garcia, M. O., Sinton, J. M., Kauahikaua, J., & Taylor, B. (2013). Intrusive dike complexes, cumulate cores, and the extrusive growth of Hawaiian volcanoes. *Geophysical Research Letters*, *40*(13), 3367–3373. https://doi.org/10.1002/grl.50633

Haslinger, F., Thurber, C., Mandernach, M., & Okubo, P. (2001). Tomographic image of P-velocity structure beneath Kilauea's East Rift zone and south flank: Seismic evidence for a deep magma body. *Geophysical Research Letters*, *28*(2), 375–378. https://doi.org/10.1029/2000gl012018

Hildenbrand, T. G., Rosenbaum, J. G., & Kauahikaua, J. P. (1993). Aeromagnetic study of the island of Hawaii. *Journal of Geophysical Research*, *98*(B3), 4099–4119. https://doi.org/10.1029/92jb02483

Jin, R., He, X., Fang, H., Xie, J., Liu, Y., & Zhang, P. (2022). Topography effect on ambient noise tomography: A case study for the Longmen Shan area, eastern Tibetan Plateau. *Geophysical Journal International*, *233*(1), 1–12. https://doi.org/10.1093/gji/ggac435

Kao, C.-Y., Osher, S., & Tsai, Y.-H. (2005). Fast sweeping methods for static Hamilton–Jacobi equations. *SIAM Journal on Numerical Analysis*, *42*(6), 2612–2632. https://doi.org/10.1137/s0036142902419600

Kauahikaua, J., Hildenbrand, T., & Webring, M. (2000). Deep magmatic structures of Hawaiian volcanoes, imaged by three-dimensional gravity models. *Geology*, *28*(10), 883–886. https://doi.org/10.1130/0091-7613(2000)028<0883:dmsohv>2.3.co;2

Köhler, A., Weidle, C., & Maupin, V. (2012). On the effect of topography on surface wave propagation in the ambient noise frequency range. *Journal of Seismology*, *16*(2), 221–231. https://doi.org/10.1007/s10950-011-9264-5

Komatitsch, D., & Tromp, J. (1999). Introduction to the spectral element method for three-dimensional seismic wave propagation. *Geophysical Journal International*, *139*(3), 806–822. https://doi.org/10.1046/j.1365-246x.1999.00967.x

Lebedev, S., & Van Der Hilst, R. D. (2008). Global upper-mantle tomography with the automated multimode inversion of surface and S-wave forms. *Geophysical Journal International*, *173*(2), 505–518. https://doi.org/10.1111/j.1365-246X.2008.03721.x

Leung, S., & Qian, J. (2006). An adjoint state method for three-dimensional transmission traveltime tomography using first-arrivals. *Communications in Mathematical Sciences*, *4*(1), 249–266. https://doi.org/10.4310/cms.2006.v4.n1.a10

Li, J., Lin, F.-C., Allam, A., Ben-Zion, Y., Liu, Z., & Schuster, G. (2019). Wave equation dispersion inversion of surface waves recorded on irregular topography. *Geophysical Journal International*, *217*(1), 346–360. https://doi.org/10.1093/gji/ggz005

Lin, F.-C., Li, D., Clayton, R. W., & Hollis, D. (2013). High-resolution 3D shallow crustal structure in Long Beach, California: Application of ambient noise tomography on a dense seismic array. *Geophysics*, *78*(4), Q45–Q56. https://doi.org/10.1190/geo2012-0453.1

Lin, F.-C., & Ritzwoller, M. H. (2011). Helmholtz surface wave tomography for isotropic and azimuthally anisotropic structure. *Geophysical Journal International*, *186*(3), 1104–1120. https://doi.org/10.1111/j.1365-246x.2011.05070.x

Lin, F.-C., Ritzwoller, M. H., & Snieder, R. (2009). Eikonal tomography: Surface wave tomography by phase front tracking across a regional broad-band seismic array. *Geophysical Journal International*, *177*(3), 1091–1110. https://doi.org/10.1111/j.1365-246x.2009.04105.x

Lin, G., Shearer, P. M., Matoza, R. S., Okubo, P. G., & Amelung, F. (2014). Three-dimensional seismic velocity structure of Mauna Loa and Kilauea volcanoes in Hawaii from local seismic tomography. *Journal of Geophysical Research: Solid Earth*, *119*(5), 4377–4392. https://doi.org/10.1002/2013jb010820

Miller, D. J. (2022). *Advances in ambient noise and coda wave seismology at Hawaiian and Aleutian arc volcanoes* (Vol. 193). ProQuest Dissertations and Theses. (Copyright - Database copyright ProQuest LLC; ProQuest does not claim copyright in the individual underlying works; Last updated - 2023-03-08). Retrieved from https://remotexs.ntu.edu.sg/user/login?url=https://www.proquest.com/dissertations-theses/advances-ambient-noise-coda-wave-seismology-at/docview/2627177868/se-2

Moore, J. G., & Clague, D. A. (1992). Volcano growth and evolution of the island of Hawaii. *Geological Society of America Bulletin*, *104*(11), 1471–1484. https://doi.org/10.1130/0016-7606(1992)104<1471:vgaeot>2.3.co;2

Ning, L., Dai, T., Wang, L., Yuan, S., & Pang, J. (2018). Numerical investigation of Rayleigh-wave propagation on canyon topography using finite-difference method. *Journal of Applied Geophysics*, *159*, 350–361. https://doi.org/10.1016/j.jappgeo.2018.09.007

Okubo, P. G., Benz, H. M., & Chouet, B. A. (1997). Imaging the crustal magma sources beneath Mauna Loa and Kilauea volcanoes, Hawaii. *Geology*, *25*(10), 867–870. https://doi.org/10.1130/0091-7613(1997)025<0867:itcmsb>2.3.co;2

Pacific Tsunami Warning Center. (1965). Pacific tsunami warning seismic system [Dataset]. International Federation of Digital Seismograph Networks. https://doi.org/10.7914/SN/PT

Park, J., Morgan, J., Zelt, C., Okubo, P., Peters, L., & Benesh, N. (2007). Comparative velocity structure of active Hawaiian volcanoes from 3-d onshore–offshore seismic tomography. *Earth and Planetary Science Letters*, *259*(3–4), 500–516. https://doi.org/10.1016/j.epsl.2007.05.008

Park, J., Morgan, J. K., Zelt, C. A., & Okubo, P. G. (2009). Volcano-tectonic implications of 3-D velocity structures derived from joint active and passive source tomography of the island of Hawaii. *Journal of Geophysical Research*, *114*(B9), B09301. https://doi.org/10.1029/2008jb005929

Pilz, M., Parolai, S., & Bindi, D. (2013). Three-dimensional passive imaging of complex seismic fault systems: Evidence of surface traces of the Issyk-Ata fault (Kyrgyzstan). *Geophysical Journal International*, *194*(3), 1955–1965. https://doi.org/10.1093/gji/ggt214

Rawlinson, N., & Sambridge, M. (2004). Wave front evolution in strongly heterogeneous layered media using the fast marching method. *Geophysical Journal International*, *156*(3), 631–647. https://doi.org/10.1111/j.1365-246x.2004.02153.x

Ritzwoller, M. H., & Levshin, A. L. (1998). Eurasian surface wave tomography: Group velocities. *Journal of Geophysical Research*, *103*(B3), 4839–4878. https://doi.org/10.1029/97jb02622

Styron, R., & Pagani, M. (2020). The GEM global active faults database. *Earthquake Spectra*, *36*(1), 160–180. https://doi.org/10.1177/8755293020944182

Taillandier, C., Noble, M., Chauris, H., & Calandra, H. (2009). First-arrival traveltime tomography based on the adjoint-state method. *Geophysics*, *74*(6), WCB1–WCB10. https://doi.org/10.1190/1.3250266

Tavakoli F, B., Operto, S., Ribodetti, A., & Virieux, J. (2017). Slope tomography based on eikonal solvers and the adjoint-state method. *Geophysical Journal International*, *209*(3), 1629–1647. https://doi.org/10.1093/gji/ggx111

Tong, P. (2021a). Adjoint-state traveltime tomography: Eikonal equation-based methods and application to the Anza area in southern California. *Journal of Geophysical Research: Solid Earth*, *126*(5), e2021JB021818. https://doi.org/10.1029/2021jb021818

Tong, P. (2021b). Adjoint-state traveltime tomography for azimuthally anisotropic media and insight into the crustal structure of central California near Parkfield. *Journal of Geophysical Research: Solid Earth*, *126*(10), e2021JB022365. https://doi.org/10.1029/2021jb022365

Tong, P., Li, T., Chen, J., & Nagaso, M. (2024). Adjoint-state differential arrival time tomography. *Geophysical Journal International*, *236*(1), 139–160. https://doi.org/10.1093/gji/ggad416

Tong, P., Yang, D., & Huang, X. (2019). Multiple-grid model parametrization for seismic tomography with application to the San Jacinto fault zone. *Geophysical Journal International*, *218*(1), 200–223. https://doi.org/10.1093/gji/ggz151

Trabant, C., Hutko, A. R., Bahavar, M., Karstens, R., Ahern, T., & Aster, R. (2012). Data products at the iris dmc: Stepping stones for research and other applications [Dataset]. Seismological Research Letters, *83*, 846–854. https://doi.org/10.1785/0220120032

Tromp, J., Tape, C., & Liu, Q. (2005). Seismic tomography, adjoint methods, time reversal and banana-doughnut kernels. *Geophysical Journal International*, *160*(1), 195–216. https://doi.org/10.1111/j.1365-246x.2004.02453.x

Tsai, Y.-H. R., Cheng, L.-T., Osher, S., & Zhao, H.-K. (2003). Fast sweeping algorithms for a class of Hamilton–Jacobi equations. *SIAM Journal on Numerical Analysis*, *41*(2), 673–694. https://doi.org/10.1137/s0036142901396533

USGS Hawaiian Volcano Observatory (HVO). (1956). Hawaiian Volcano Observatory Network [Dataset]. International Federation of Digital Seismograph Networks. https://doi.org/10.7914/SN/HV

Wang, J., Wu, G., & Chen, X. (2019). Frequency-Bessel transform method for effective imaging of higher-mode Rayleigh dispersion curves from ambient seismic noise data. *Journal of Geophysical Research: Solid Earth*, *124*(4), 3708–3723. https://doi.org/10.1029/2018jb016595

Wang, K., Yang, Y., Basini, P., Tong, P., Tape, C., & Liu, Q. (2018). Refined crustal and uppermost mantle structure of southern California by ambient noise adjoint tomography. *Geophysical Journal International*, *215*(2), 844–863. https://doi.org/10.1093/gji/ggy312

Wang, K., Yang, Y., Jiang, C., Wang, Y., Tong, P., Liu, T., & Liu, Q. (2021). Adjoint tomography of ambient noise data and teleseismic p waves: Methodology and applications to central California. *Journal of Geophysical Research: Solid Earth*, *126*(6), e2021JB021648. https://doi.org/10.1029/2021jb021648

Wei, X., & Shen, Y. (2022). P waves emerged from ambient noise cross-correlation post the 2018 Kılauea eruption revealing middle crust velocity discontinuities beneath the island of Hawaii. *Geophysical Research Letters*, *49*(16), e2022GL098470. https://doi.org/10.1029/2022gl098470

Wei, X., Shen, Y., & Morgan, J. K. (2023). Shallow volcano-tectonic structures on the island of Hawai'i imaged by multimode Rayleigh wave ambient noise tomography. *Journal of Geophysical Research: Solid Earth*, *128*(5), e2022JB026244. https://doi.org/10.1029/2022JB026244

Wessel, P., Luis, J., Uieda, L., Scharroo, R., Wobbe, F., Smith, W. H., & Tian, D. (2019). The generic mapping tools version 6 [Software]. Geochemistry, Geophysics, Geosystems, *20*, 5556–5564. https://doi.org/10.1029/2019GC008515

Xia, J. (2014). Estimation of near-surface shear-wave velocities and quality factors using multichannel analysis of surface-wave methods. *Journal of Applied Geophysics*, *103*, 140–151. https://doi.org/10.1016/j.jappgeo.2014.01.016

Xie, J., Yang, Y., & Luo, Y. (2020). Improving cross-correlations of ambient noise using an RMS-ratio selection stacking method. *Geophysical Journal International*, *222*(2), 989–1002. https://doi.org/10.1093/gji/ggaa232

Yao, H., van Der Hilst, R. D., & De Hoop, M. V. (2006). Surface-wave array tomography in SE Tibet from ambient seismic noise and two-station analysis—I. Phase velocity maps. *Geophysical Journal International*, *166*(2), 732–744. https://doi.org/10.1111/j.1365-246x.2006.03028.x

Zhao, P., Campillo, M., Chen, J., Liu, Q., Li, Y., & Guo, B. (2020). Topographic correction in ambient noise tomography. *Chinese Journal of Geophysics*, *63*(10), 3764–3774.

Zucca, J. J., Hill, D. P., & Kovach, R. L. (1982). Crustal structure of Mauna Loa volcano, Hawaii, from seismic refraction and gravity data. *Bulletin of the Seismological Society of America*, *72*(5), 1535–1550.